

Fully quantum description of the Zundel ion: combining variational quantum Monte Carlo with path integral Langevin dynamics

Félix Mouhat,¹ Sandro Sorella,² Rodolphe Vuilleumier,³ Antonino Marco Saitta,¹ and Michele Casula¹

¹*IMPMC, Sorbonne Universités, Université Pierre et Marie Curie,
CNRS, IRD, MNHN, 4 place Jussieu, 75252 Paris, France**

²*International School for Advanced Studies (SISSA), Via Bonomea 26, 34136 Trieste,
Italy and INFN Democritos National Simulation Center, 34151 Trieste, Italy*

³*Pôle de Physico-chimie Théorique de l'ENS, Laboratoire PASTEUR - UMR CNRS 8640, 24 rue Lhomond, 75005 Paris, France*
(Dated: June 18, 2019)

We introduce a novel approach for a fully quantum description of coupled electron-ion systems from first principles. It combines the variational quantum Monte Carlo solution of the electronic part with the path integral formalism for the quantum nuclear dynamics. On the one hand, the path integral molecular dynamics includes nuclear quantum effects by adding a set of fictitious classical particles (beads) aimed at reproducing nuclear quantum fluctuations via a harmonic kinetic term. On the other hand, variational quantum Monte Carlo can provide Born-Oppenheimer potential energy surfaces with a precision comparable to the most advanced post Hartree-Fock approaches, and with a favorable scaling with the system size. In order to deal with the intrinsic noise due to the stochastic nature of quantum Monte Carlo methods, we generalize the path integral molecular dynamics using a Langevin thermostat correlated according to the covariance matrix of quantum Monte Carlo nuclear forces. The variational parameters of the quantum Monte Carlo wave function are evolved during the nuclear dynamics, such that the Born-Oppenheimer potential energy surface is unbiased. Statistical errors on the wave function parameters are reduced by resorting to bead grouping average, which we show to be accurate and well controlled. Our general algorithm relies on a Trotter breakup between the dynamics driven by ionic forces and the one set by the harmonic interbead couplings. The latter is exactly integrated even in presence of the Langevin thermostat, thanks to the mapping onto an Ornstein-Uhlenbeck process. This framework turns out to be very efficient also in the case of noiseless (deterministic) ionic forces. The new implementation is validated on the Zundel ion (H_5O_2^+) by direct comparison with standard path integral Langevin dynamics calculations made with a coupled cluster potential energy surface. Nuclear quantum effects are confirmed to be dominant over thermal effects well beyond room temperature giving the excess proton an increased mobility by quantum tunneling.

I. INTRODUCTION

In spite of about half a century of numerical investigations aimed at providing a quantitative and reliable microscopic description of liquid water, there is still a difficulty in describing accurately proton hopping inside the strong and well structured hydrogen bond network giving water its numerous peculiar features. Since water is the solvent of most chemical and biological processes occurring on Earth, one of the long-term goals is to explicitly take into account, at a high accuracy level, hydrogen-bond driven phenomena in the treatment of species interacting with this solvent. The solvation and transport properties of hydronium (H_3O^+) and hydroxide (HO^-) ions in aqueous environment have enormous impacts on areas ranging from aqueous acid-base chemistry^{1–6}, enzymatic proton transfer^{7,8}, as well as proton transfer in biological channels⁹, through fuel cell membranes^{10,11} and on ice surfaces facilitating atmospheric reactions¹². Recent progress in our understanding of proton transport in water has been reviewed in Refs.13 and 14.

Due to a variety of interactions present in water such as weak and dispersive dipolar interactions that compete during the formation and the breaking of hydrogen bonds inside a strongly polar network, an accurate description of the Potential Energy Surface (PES) is re-

quired to fully understand the microscopic properties of water. From a theoretical point of view, liquid water has been studied through Molecular Dynamics (MD) techniques such as the empirical force fields methods^{15–17} and *ab initio* molecular dynamics (AIMD)^{18–23}. Because of its good scalability with the system size which is suited to study liquids, Density Functional Theory (DFT) has been the most employed technique to perform AIMD simulations of bulk water. Nevertheless, DFT-based calculations performed with Generalized Gradient Approximation (GGA) functionals give rise to an over-structuration of water: melting point temperature²⁴ and oxygen-oxygen radial distribution function²⁵ are for instance poorly reproduced. Some improvements by including Van der Waals corrections such as the BLYP-DCACP, BLYP- $\text{D}_{\text{G}2}$ or PBE0+TS-vdW(SC) functionals have been tested and proven to get results closer to experiments^{26,27} but these approaches suffer from a lack of generality and transferability. Gillan *et al.* recently established a numerical scoring system to evaluate the quality of different exchange-correlation functionals for a wide range of water systems²⁸.

As an alternative to DFT-AIMD, very accurate calculations using embedded-fragment second-order Møller-Plesset perturbation theory (MP2) have been carried out and gave satisfactory results despite the shortness of the

MD trajectories (6 ps of equilibration and 5 ps of production run)²⁹. Perturbative theories such as MP2/MP4 or the most advanced quantum chemistry techniques such as Coupled Cluster (CC) calculations are indeed suffering from a poor scalability with the number of particles N in the system. Thus, the field of interest of these methods is typically the study of electronic properties at zero temperature and structural relaxations of small systems.

Quantum Monte Carlo (QMC) techniques constitute a very interesting alternative to study aqueous systems, since the scalability of the method (N^{3-4}) makes the simulations of very large systems computationally affordable with a much greater accuracy than DFT in most cases. Recently, it has been demonstrated that QMC techniques provide results as accurate as the basis set converged Coupled Cluster (CCSD(T)) for small neutral or charged water clusters^{30,31}. Consequently, QMC can now be used as a benchmark method and certainly benefits from its intrinsically parallel formulation in modern supercomputers. The price to pay here is the systematic statistical incertitude arising from the stochastic nature of the QMC approach, which can however be reduced by generating longer Markov chains as the error is inversely proportional to the square root of the number of QMC generations.

Some strategies have thus been developed to incorporate the intrinsic QMC noise into a classical statistical mechanics framework of nuclei at finite temperature T . For instance, the Coupled Electron Ion Monte Carlo (CEIMC) method relies on the Born-Oppenheimer (BO) approximation for treating finite temperature ions coupled with ground state electrons. The Boltzmann distribution function of the ionic degrees of freedom is sampled at fixed temperature via a Metropolis MC simulation based on the electronic energies computed during independent ground state QMC calculations^{32,33}. Another strategy is to resort to a Langevin MD approach to correlate the noise driving the Langevin Dynamics (LD) of the system by the QMC forces covariance. In that case, the wave function parameters are optimized by Variational Monte Carlo (VMC) calculations along the MD path such that the electronic solution has always energies and forces as close as possible to the true BO surface^{34,35}.

Last year, Zen and coworkers applied the latter method to perform the very first QMC-based MD simulation of bulk liquid water at ambient conditions using 32 water molecules in a cubic cell with periodic boundary conditions³⁶. By obtaining a better position of the first peak of the oxygen-oxygen radial distribution function compared with most advanced functionals, they demonstrated the ability of QMC to tackle this kind of problems. However, the authors had to make some approximations: they expanded the wave function over a small basis set and more importantly a classical description of the nuclei was adopted.

Indeed, it is well known that Nuclear Quantum Effects (NQE) play a crucial role in the description of water or ice by deeply affecting the radial distribution func-

tions and distorting hydrogen bonds because of quantum disorder³⁷⁻⁴¹. In this paper, we propose to extend Zen's pioneering work by including a nuclear quantum description within the QMC-driven dynamics. This is achieved within a Path Integral Langevin Dynamics (PILD) approach which, to the best of our knowledge, has never been used in the case of non-deterministic forces.

On the one hand, we derive an original algorithm to integrate the Langevin equations of motion for quantum particles. The designed algorithm is very general since it can be used to propagate both deterministic and stochastic forces. On the other hand, within our framework we show that the inclusion of the quantum nature of the nuclei in the QMC-driven MD does not slow down the simulation with respect to the classical counterpart. This is thanks to an effective average of wave function parameters in the polymer representation of quantum nuclei, which relies upon a bead-grouping technique. Therefore, the cost of the wave function optimization is not increased by the inclusion of the additional quantum degrees of freedom.

To test our methodological development, we apply it to H_5O_2^+ , namely the Zundel ion⁴², widely used as benchmark system. Indeed, it is the simplest system to exhibit a non trivial proton transfer and its reduced size makes a comprehensive and systematic study of the problem easier. More importantly, there is a huge amount of data⁴³⁻⁵² to compare our results with, because this system has been massively studied both theoretically and experimentally in the last fifty years. We can cite for instance the extremely accurate Potential Energy Surface (PES) generated by Bowman and coworkers from almost exact CCSD(T) calculations⁵³. Moreover, because of the great importance of the NQE in this system, it is almost always used to test and validate new approaches. For example, Ceriotti and coworkers studied this system to validate their novel multiple time steps integrator to accelerate MD by including NQE at low cost using a thermostat which works with a colored noise⁵⁴.

The paper is organized as follows. In Section II, we introduce the theoretical framework by first reviewing the algorithms for classical Langevin simulations with QMC forces (Secs. IIA and IIB). In Secs. IIC and IID we extend the classical description of nuclei by introducing original and efficient algorithms to integrate the equations of motion in the nuclear quantum case with or without noisy forces. A study of the numerical stability of the new path integral integrators is done in Sec. IIE for deterministic forces, where a direct comparison with existing PILD algorithms is possible. The inclusion of QMC forces is discussed in Sec. III. The general form of the QMC wave function for the electronic part is described in Sec. IIIA, the bead-grouping approximation is introduced in Sec. IIIB, a short review on the QMC ionic force evaluation is provided in Sec. IIIC, while the QMC-noise correction scheme is detailed in Sec. IIID, which yields an unbiased sampling of the canonical quantum partition function even in the presence of stochastic errors.

Sec. III E reports on the numerical stability analysis of the new integrators with noisy QMC forces. In Section IV, we show the results obtained for the Zundel ion at low and room temperatures by taking into account, or not, the NQE and demonstrate the excellent agreement between the noisy QMC PES and the very accurate deterministic CCSD(T) one, which validates our method. Finally, in Section V, we provide some concluding remarks and we discuss the possible future applications of the algorithms developed in this paper.

II. METHODS

In this Section, we derive the methodology to sample the canonical partition function corresponding to Hamiltonians including either classical or quantum nuclei. This is achieved using the generalized Langevin dynamics, which has been demonstrated to be compatible with the path integral approach to include a quantum description of the nuclei⁵⁵. Thanks to the stochastic nature of this category of non-Newtonian dynamics, the Langevin formulation of the equations of motion can be extended to the QMC case, where the forces are intrinsically noisy^{34,35}.

A. Classical Langevin Dynamics: basic algorithm

Let us consider a system constituted by N classical particles described by the Hamiltonian

$$H = \sum_{i=1}^{3N} \frac{p_i^2}{2m_i} + V(q_1, \dots, q_{3N}), \quad (1)$$

where p_i and q_i are the atomic momenta and positions, respectively, and V is the PES in which the system evolves. Hereafter, we are going to use transformed variables, more convenient to manipulate, achieved by the following mass scaling:

$$\begin{aligned} q_i &= q_i^0 \sqrt{m_i} \\ p_i &= p_i^0 / \sqrt{m_i} \\ \eta_i &= \eta_i^0 \sqrt{m_i} \\ f_i &= f_i^0 / \sqrt{m_i}, \end{aligned} \quad (2)$$

where $\{q_i^0, p_i^0, \eta_i^0, f_i^0\}_{i=1, \dots, 3N}$ are the original coordinates and $\{q_i, p_i, \eta_i, f_i\}_{i=1, \dots, 3N}$ denote the transformed ones. After applying the above transformation, the corresponding second order Langevin dynamics reads:

$$\dot{\mathbf{p}} = -\gamma \mathbf{p} + \mathbf{f}(\mathbf{q}) + \boldsymbol{\eta}(t) \quad (3)$$

$$\dot{\mathbf{q}} = \mathbf{p}, \quad (4)$$

where $\mathbf{f} = -\nabla_{\mathbf{q}} V(\mathbf{q})$ is the applied force deriving from the PES, and the vectors are $3N$ -dimensional. To ensure that the equilibrium distribution generated by this dynamics is canonical, the r.h.s of Eq. (3) includes a

$3N \times 3N$ friction matrix γ and a random force vector $\boldsymbol{\eta}$. The latter controls the temperature T of the system via the Fluctuation-Dissipation Theorem (FDT)⁵⁶

$$\gamma = \frac{\alpha}{2k_B T}, \quad (5)$$

with k_B the Boltzmann constant, and

$$\alpha_{ij} \delta(t - t') = \langle \eta_i(t) \eta_j(t') \rangle \quad (6)$$

is the force covariance matrix which simply reduces to a diagonal form for white noise^{57,58}. The dynamics generated by the stochastic differential Eqs. (3) and (4) is Markovian, as the noise fluctuations are locally correlated in time. In the case the ionic forces are computed by QMC methods (as we will see in Sec. III D), the covariance matrix has non-trivial off-diagonal elements, and $\boldsymbol{\eta}$ fluctuations are correlated by the QMC statistics. Thus, the Langevin approach can naturally deal with noisy QMC forces, as already shown by Sorella and coworkers in the classical MD framework³⁴⁻³⁶.

Eq. (3) belongs to a general class of Stochastic Differential Equations (SDEs), whose solution is explicit whenever both the friction matrix and the force are independent of q ⁵⁹

$$\mathbf{p}(t') = e^{-\gamma(t'-t)} \mathbf{p}(t) + \int_t^{t'} ds e^{\gamma(s-t)} (\mathbf{f} + \boldsymbol{\eta}(s)). \quad (7)$$

Starting from this form, Attaccalite *et al.*³⁴ proposed to use this integration algorithm in a QMC-based MD, because in short time interval $t' - t = \delta t$ the q -dependence of the force and the friction can be neglected and can be assumed to remain at their initial values $\mathbf{f}(t)$ and $\gamma(t)$, leading to an explicit integration of the LD at discrete equally spaced times $t_n = n\delta t$:

$$\mathbf{p}_{n+1} = e^{-\gamma_n \delta t} \mathbf{p}_n + \Gamma(\mathbf{f}_n + \tilde{\boldsymbol{\eta}}) \quad (8)$$

$$\mathbf{q}_{n+1} = \mathbf{q}_n + \mathbf{p}_n \delta t, \quad (9)$$

where the time evolution has been discretized with time step δt , and the subscripts refer to the corresponding time slice, such that $\mathbf{p}_n = \mathbf{p}(t_n)$, $\mathbf{q}_n = \mathbf{q}(t_n)$, and $\mathbf{f}_n = \mathbf{f}(\mathbf{q}(t_n))$. In the above Equations, the Γ matrix is defined as

$$\Gamma = \gamma_n^{-1} (1 - e^{-\gamma_n \delta t}), \quad (10)$$

and it multiplies the forces \mathbf{f} under the approximation that δt is small enough to disregard the time dependence of $\mathbf{f}(\mathbf{q})$ in Eq. (7). In the same interval δt , the time dependent noise $\boldsymbol{\eta}(t)$ is integrated, leading to the stochastic variable $\tilde{\boldsymbol{\eta}}$, whose mean and variance-covariance are

$$\langle \tilde{\boldsymbol{\eta}} \rangle = 0,$$

$$\langle \tilde{\boldsymbol{\eta}}^T \tilde{\boldsymbol{\eta}} \rangle = k_B T \gamma_n^2 \coth\left(\gamma_n \frac{\delta t}{2}\right), \quad (11)$$

respectively. These relations have been derived directly from the FDT (5), with the hypothesis that the fluctuations are local in time (6).

The time step δt and the friction matrix γ are algorithmic parameters to be defined in order to carry out the classical LD based on this scheme. If the forces are deterministic, γ can take a diagonal form, such that $\gamma_{ij} = \gamma_{\text{BO}} \delta_{ij}$, with γ_{BO} a value appropriately chosen to optimize the efficiency of the canonical sampling. According to Eq. (11), this implies a diagonal $\langle \tilde{\eta}^T \tilde{\eta} \rangle$, i.e. a non-correlated noise. In the case of noisy forces, $\tilde{\eta}$ can be separated into a contribution $\delta \mathbf{f}$ (*already* included in the QMC forces \mathbf{f}) and $\tilde{\eta}^{\text{ext}}$. The latter contribution has to be explicitly added in Eq. (8), such that its covariance added to the external noise variance satisfies: $\langle (\tilde{\eta}^{\text{ext}})^T \tilde{\eta}^{\text{ext}} \rangle + \langle \delta \mathbf{f}^T \delta \mathbf{f} \rangle = \langle \tilde{\eta}^T \tilde{\eta} \rangle$, where $\langle \tilde{\eta}^T \tilde{\eta} \rangle$ is given by Eq. (11) and $\langle \delta \mathbf{f}^T \delta \mathbf{f} \rangle$ is the QMC force covariance, which will have in general non-zero off-diagonal matrix elements. Thus, if the forces are noisy γ is non-diagonal, as discussed in Sec. III D. In that case, one has to rotate the momenta and positions in the frame which diagonalizes γ , in order to perform numerically the Markov iteration in Eqs. (8) and (9).

B. Classical Langevin Dynamics: Classical Momentum-Position Correlator (CMPC) algorithm

The previous basic algorithm has been further developed in Ref. 35 and later in Ref. 36, to improve the integration of the positions \mathbf{q} in Eq. (9), by taking into account the evolution of $\mathbf{p}(t)$ during the time interval δt . Here, we provide an alternative derivation, based on the joint momentum-position coordinates

$$\mathbf{X} = \begin{pmatrix} \mathbf{p} \\ \mathbf{q} \end{pmatrix}, \quad (12)$$

where \mathbf{X} is a $6N$ -dimensional vector. Analogously, we extend the definition of the ionic and random force vectors to be $\mathbf{F} = \begin{pmatrix} \mathbf{f} \\ \mathbf{0} \end{pmatrix}$ and $\mathbf{E} = \begin{pmatrix} \boldsymbol{\eta} \\ \mathbf{0} \end{pmatrix}$, respectively. In this extended basis, Eqs. (3) and (4) can be rewritten into a generalized SDE, which reads as

$$\dot{\mathbf{X}} = -\hat{\gamma} \mathbf{X} + \mathbf{F} + \mathbf{E}, \quad (13)$$

where in this notation the matrix $\hat{\gamma}$ represents a generalized friction that couples both momenta and positions by:

$$\hat{\gamma} = \begin{pmatrix} \gamma & \mathbf{0} \\ -\mathbf{I} & \mathbf{0} \end{pmatrix}, \quad (14)$$

with the “physical” friction γ being the same $3N \times 3N$ matrix introduced in Eq. (3), and \mathbf{I} is the identity matrix. Analogously to Eq. (7), the formal solution of (13) is provided by

$$\mathbf{X}(t') = e^{-\hat{\gamma}(t'-t)} \mathbf{X}(t) + \int_t^{t'} ds e^{\hat{\gamma}(s-t')} (\mathbf{F}(\mathbf{X}(s)) + \mathbf{E}(s)). \quad (15)$$

Using joint coordinates would be of little use, if we were not able to evaluate the exponential $e^{-\hat{\gamma}\delta t}$ in a closed analytic form. Indeed, this is possible because the block matrix $\hat{\gamma}$ can be more conveniently rewritten in terms of Pauli matrices $\sigma_x, \sigma_y, \sigma_z$, as follows:

$$\hat{\gamma} = \frac{\gamma}{2} \otimes \mathbf{I} - \frac{\mathbf{I}}{2} \otimes \sigma_x + i \frac{\mathbf{I}}{2} \otimes \sigma_y + \frac{\gamma}{2} \otimes \sigma_z. \quad (16)$$

Then, the exponentiation can be straightforwardly obtained by using standard Pauli matrices algebra, and the solution can be given in a closed form:

$$\mathbf{p}_{n+1} = e^{-\gamma\delta t} \mathbf{p}_n + \mathbf{\Gamma} (\mathbf{f}_n + \tilde{\eta}) \quad (17)$$

$$\mathbf{q}_{n+1} = \mathbf{q}_n + \mathbf{\Gamma} \mathbf{p}_n + \mathbf{\Theta} (\mathbf{f}_n + \tilde{\eta}), \quad (18)$$

with $\mathbf{\Gamma}$ previously defined in Eq. (10), and

$$\mathbf{\Theta} = \gamma^{-2} (-1 + \gamma\delta t + e^{-\gamma\delta t}), \quad (19)$$

$$\tilde{\eta} = \mathbf{\Gamma}^{-1} \int_{t_n}^{t_{n+1}} dt e^{\gamma(t-t_{n+1})} \boldsymbol{\eta}(t), \quad (20)$$

$$\tilde{\tilde{\eta}} = (\mathbf{\Theta} \gamma)^{-1} \int_{t_n}^{t_{n+1}} dt (1 - e^{\gamma(t-t_{n+1})}) \boldsymbol{\eta}(t). \quad (21)$$

We immediately notice that the present algorithm differs from those developed in literature^{60–65}, since momenta and positions are propagated simultaneously in a single iteration thanks to the use of momentum-position correlation matrices. In particular, according to Eqs. (17) and (18), not only the momenta but also the positions are affected by the integrated Langevin noise, $\tilde{\eta}$ and $\tilde{\tilde{\eta}}$. Their variance-covariance can be computed by imposing the FDT (5) to be fulfilled, under the hypothesis that the α matrix is \mathbf{q} -time independent (as we have done in Sec. II A), and by exploiting that $[\alpha, \gamma] = 0$. One finds:

$$\begin{aligned} \tilde{\alpha}_{11} &= \langle \tilde{\eta}^T \tilde{\eta} \rangle = k_B T \gamma^2 \coth \left(\gamma \frac{\delta t}{2} \right), \\ \tilde{\alpha}_{22} &= \langle \tilde{\tilde{\eta}}^T \tilde{\tilde{\eta}} \rangle = k_B T (2\mathbf{\Theta} - \mathbf{\Gamma}^2) \mathbf{\Theta}^{-2}, \\ \tilde{\alpha}_{12} &= \langle \tilde{\eta}^T \tilde{\tilde{\eta}} \rangle = \tilde{\alpha}_{21} = \langle \tilde{\tilde{\eta}}^T \tilde{\eta} \rangle = k_B T \gamma \mathbf{\Gamma} \mathbf{\Theta}^{-1}, \end{aligned} \quad (22)$$

while the mean of $\tilde{\eta}$ and $\tilde{\tilde{\eta}}$ is zero. It is interesting to note that the momentum-position correlator formalism correlates the integrated noise, even without dealing with non-diagonal α matrices, as we will do in the QMC case. We also remark that in order to derive the integrated equations of motion (17) and (18), we have made the same approximation as in Sec. II A, as far as the ionic forces \mathbf{f} are concerned. Indeed, in Eq. (15) we disregarded the \mathbf{q} -time dependence of \mathbf{f} in the time interval δt . For deterministic forces, where α is position independent, it is the only approximation left in the classical Langevin dynamics driven by (17) and (18).

As in the basic algorithm of Sec. II A, $\gamma_{ij} = \gamma_{\text{BO}} \delta_{ij}$ for deterministic \mathbf{f} , while the definition of γ is more general

for noisy QMC forces (see Sec. III). Once γ and δt have been set, the numerical evolution is performed according to Eqs. (17) and (18) in the frame which diagonalizes γ .

C. Path Integral Langevin Dynamics: Path Integral Momentum-Position Correlator (PIMPC) algorithm

As we mentioned in the Introduction, it is well known that NQE are extremely important, in liquid water and aqueous species such as the Zundel ion, because of the light mass of the hydrogen atom. NQE are consequently essential to ensure a good description of both quantum and thermal fluctuations of the hydrogen bond network and must be taken into account since they dramatically modify the effective energy landscape of the problem. Several approaches to deal with NQE have been proposed so far, such as the Quantum Thermal Bath (QTB)^{66–68}, but we have chosen here to focus on the Path Integral (PI) framework for the following reasons. First, the formulation of the theory is intrinsically parallel and perfectly compatible with the QMC multi-walker implementation. This constitutes a major advantage to perform highly-parallel simulations for High Performance Computing (HPC) applications. Second, the PI relies on approximations which are systematically improvable and the exact result can be recovered with controlled extrapolations. Third, this approach can be easily combined with the LD leading to the PILD method, for which very efficient algorithms already exist^{69,70}.

We first recall the basic formalism of the PIMD method (see Ref. 69 for further details), before introducing our approach to propagate the corresponding equations of motion. In PI theory, the quantum partition function $Z = \text{Tr} [e^{-\beta H}]$ (with $\beta = 1/k_B T$) is usually approximated after a standard Trotter factorization⁷¹ by

$$Z \simeq \frac{1}{(2\pi\hbar)^f} \int d^f \mathbf{p} d^f \mathbf{q} e^{-\tau H_M(\mathbf{p}, \mathbf{q})}, \quad (23)$$

with $f = MN$ and $\tau = \beta/M$. We have replaced here the true quantum particles by fictitious classical ring polymers consisting of M replicas (beads) of the system connected to each other by harmonic springs evolving in the imaginary time τ . Without loss of generality, we can extend the definition of classical vectors to the quantum case, by including all M replicas in the string, such that $\mathbf{q} \equiv (\mathbf{q}^{(1)}, \dots, \mathbf{q}^{(i)}, \dots, \mathbf{q}^{(M)})^T$ and it becomes $3NM$ -dimensional. Bold vectors will automatically include all replicas in the quantum case. If interpreted classically, the partition function Z in Eq. (23) describes a system at the effective temperature MT . The Hamiltonian H_M corresponding to this quantum-to-classical isomorphism

reads as

$$H_M(\mathbf{p}, \mathbf{q}) = \sum_{i=1}^{3N} \sum_{j=1}^M \left(\frac{1}{2} [p_i^{(j)}]^2 + \frac{1}{2} \tilde{\omega}_M^2 (q_i^{(j)} - q_i^{(j-1)})^2 \right) + \sum_{j=1}^M V(q_1^{(j)}, \dots, q_{3N}^{(j)}), \quad (24)$$

written in mass-scaled coordinates (2), with $\tilde{\omega}_M = M/\beta\hbar$, and subjected to the ring boundary condition $q_i^{(0)} \equiv q_i^{(M)}$. Thus, the PIMD method is a way to calculate quantum mechanical properties using the recipes from classical statistical mechanics with a modified Hamiltonian containing an additional quantum kinetic term. Using the well-known formula for a generic observable A

$$\langle A \rangle = \frac{1}{Z} \text{Tr} [e^{-\beta H} A], \quad (25)$$

it is straightforward to evaluate the potential energy of the system:

$$\langle V \rangle \simeq \frac{1}{(2\pi\hbar)^f Z} \int d^f \mathbf{p} d^f \mathbf{q} e^{-\tau H_M(\mathbf{p}, \mathbf{q})} V_M(\mathbf{q}), \quad (26)$$

where $V_M(\mathbf{q}) = \frac{1}{M} \sum_{j=1}^M V(q_1^{(j)}, \dots, q_{3N}^{(j)})$ is the bead-dependent potential averaged over all the replicas. The quantum kinetic energy can also be evaluated according to

$$\langle T \rangle \simeq \frac{1}{(2\pi\hbar)^f Z} \int d^f \mathbf{p} d^f \mathbf{q} e^{-\tau H_M(\mathbf{p}, \mathbf{q})} T_M(\mathbf{q}), \quad (27)$$

where $T_M(\mathbf{q})$ is most often chosen to be the centroid virial estimator,

$$T_{M,\text{vir}}(\mathbf{q}) = \frac{N}{2\beta} + \frac{1}{2M} \sum_{i=1}^{3N} \sum_{j=1}^M (q_i^{(j)} - \bar{q}_i) \partial_{q_i^{(j)}} \tilde{V}, \quad (28)$$

with $\bar{q}_i = \frac{1}{M} \sum_{j=1}^M q_i^{(j)}$, $\partial_{q_i^{(j)}} \equiv \frac{\partial}{\partial q_i^{(j)}}$ and $\tilde{V} = \sum_{j=1}^M V(q_1^{(j)}, \dots, q_{3N}^{(j)}) = MV_M$. Let us notice that it is not the only way to estimate the quantum kinetic energy. Indeed, a more noisy and therefore less convenient estimator is obtained with the primitive approximation, yielding:

$$T_{M,\text{pri}}(\mathbf{q}) = \frac{3NM}{2\beta} - \frac{1}{M} \sum_{j=1}^M \frac{1}{2} \left(\frac{q_i^{(j)} - q_i^{(j-1)}}{\hbar\tau} \right)^2. \quad (29)$$

It is clear from Eq. (29) that the primitive estimator is more difficult to control because of the negative contributions that can become important when some paths are more spread out than they should. This apparent drawback actually gives precious information about the quality of the quantum sampling over the paths since one

should obtain $\langle T \rangle_{\text{vir}} = \langle T \rangle_{\text{pri}}$ in fully converged calculations in the limit $\delta t \rightarrow 0$ for any value of M . In practice this is almost never met exactly and it is particularly difficult to fulfill it for large M . Indeed, two constraints limit the choice of M . On one side, M must be large enough to recover all quantum properties of the physical system; on the other side, M should not be too large, otherwise the quantum imaginary time $\tau = \beta/M$ would become too small and too large fluctuations in the primitive energy evaluation would appear.

By making the choice of Parrinello and Rahman to set the physical masses for each ring polymer bead, we are using the Ring Polymer Molecular Dynamics (RPMD) approximation to real quantum correlation functions⁷², although real-time properties are lost when a thermostat is applied to the system, as we shall do in the following. Various choices are available for the thermostat, ranging from the more conventional Nosé-Hoover chain^{73,74} to stochastic thermostating in both its simple path integral Langevin equation (PILE) form⁶⁹, which fulfills the FDT, and its Generalized Langevin Equation (GLE) flavors^{55,69,75}, where the noise is colored to simulate quantum effects and accelerate the convergence of the PIMD with the number of beads, at the price of breaking the validity of the FDT. Here, we would like to take the Langevin approach of stochastic thermostat, fulfilling the FDT, in order to sample the PI canonical distribution in Eq. (23). This is the so-called “standard” PILD approach. However, instead of using the PILE integration algorithm⁶⁹, we will extend our classical Momentum-Position Correlator (MPC) algorithm, described in Sec. II B, to the quantum case. As already mentioned, this framework will allow us to incorporate noisy QMC forces in the equations of motion, by using an appropriately tailored Langevin noise without breaking the FDT, as it is explained in Sec. III. Moreover, in our final algorithm, which makes use of a Trotter breakup⁷¹ between the harmonic and the physical modes, the quantum harmonic part is integrated exactly together with the Langevin thermostat for the harmonic frequencies. Indeed, the corresponding Langevin equations of motion are linear. It is then possible to exploit the mapping onto an Ornstein-Uhlenbeck process (OUP), which is exactly integrable, as explained in Sec. II D.

We start by applying the same idea as of our classical algorithm with momentum-position correlators to the quantum-to-classical mapping Hamiltonian described in Eq. (24). The equations of motion for H_M can be rewritten in the same form as in the Eq. (13), provided \mathbf{X} is now interpreted as a $6NM$ -dimensional vector, the thermal noise $\boldsymbol{\eta}$ lives in the $3NM$ -dimensional space, and the ionic forces are defined such as $\mathbf{f} \equiv \{f_i^{(j)}\}_{i=1,\dots,3N}^{j=1,\dots,M}$, where $f_i^{(j)} = -\partial_{q_i^{(j)}} \tilde{V}$. The main difference with respect to the classical formalism is in the generalized friction $\hat{\gamma}$, which must be redefined in order to include the harmonic couplings between the beads. $\hat{\gamma}$ is now a $6NM \times 6NM$

matrix, which reads as

$$\hat{\gamma} = \begin{pmatrix} \gamma & \mathbf{K} \\ -\mathbf{I} & \mathbf{0} \end{pmatrix}, \quad (30)$$

where \mathbf{K} is $3NM \times 3NM$ matrix defined as follows:

$$K_{ih}^{(j)(k)} = \tilde{\omega}_M^2 \delta_{ih} \left(2\delta^{(j)(k)} - \delta^{(j)(k-1)} - \delta^{(j)(k+1)} \right). \quad (31)$$

In the above definition, we have used lower indexes to indicate the particle components, the upper ones (in parenthesis) indicate the bead components, while δ_{ij} ($\delta^{(i)(j)}$ for the bead indexes) is the usual Kronecker delta. The \mathbf{K} matrix is diagonal in the particle sector, as the harmonic springs in the fictitious H_M (24) couple different replicas only for the same particle components. Cyclic conditions are implicitly applied in Eq. (31) to the matrix boundaries in the bead sector (i.e. $(0) = (M)$), as the polymers are necklaces.

As we have done in Eq. (16) for the classical case, we expand $\hat{\gamma}$ in Pauli matrices, as follows:

$$\hat{\gamma} = \frac{\gamma}{2} \otimes \mathbf{I} + \frac{\mathbf{K} - \mathbf{I}}{2} \otimes \sigma_x + i \frac{\mathbf{K} + \mathbf{I}}{2} \otimes \sigma_y + \frac{\gamma}{2} \otimes \sigma_z. \quad (32)$$

Moreover, we require that $[\mathbf{K}, \boldsymbol{\gamma}] = 0$, which is fulfilled when the forces \mathbf{f} are deterministic. Indeed, $\boldsymbol{\gamma}$ obeys the FDT (5) in the extended $3NM$ dimensional space. For deterministic forces, $\boldsymbol{\gamma}$ is bead independent, while for noisy forces the matrix $\boldsymbol{\alpha}$ could be correlated according to the force covariance $\langle \delta f_i^{(j)} \delta f_h^{(k)} \rangle$, and $\boldsymbol{\gamma}$ could acquire a bead dependent contribution to fulfill the FDT. For the time being, let us assume $\boldsymbol{\gamma}$ to be bead independent, which implies that \mathbf{K} and $\boldsymbol{\gamma}$ commute. We will see in Sec. III D how to recover this condition even in the case of QMC forces. Then, Eq. (32) and $[\mathbf{K}, \boldsymbol{\gamma}] = 0$ allow one to evaluate $e^{\hat{\gamma}\delta t}$ in a closed analytic form for each (upper and lower) block component of the SDE formal solution in Eq. (15). The related algebra is quite tedious and we refer the reader to the Appendix B. The resulting integrated equations of motions lead to the following Markov chain:

$$\begin{aligned} \mathbf{p}_{n+1} &= \boldsymbol{\Lambda}_{1,1} \mathbf{p}_n + \boldsymbol{\Lambda}_{1,2} \mathbf{q}_n + \boldsymbol{\Gamma} (\mathbf{f}_n + \tilde{\boldsymbol{\eta}}), \\ \mathbf{q}_{n+1} &= \boldsymbol{\Lambda}_{2,1} \mathbf{p}_n + \boldsymbol{\Lambda}_{2,2} \mathbf{q}_n + \boldsymbol{\Theta} (\mathbf{f}_n + \tilde{\boldsymbol{\eta}}), \end{aligned} \quad (33)$$

with the integrated $6NM$ -dimensional noise (\mathbf{E}_{int}) and force (\mathbf{F}_{int}) which are, respectively,

$$\mathbf{E}_{\text{int}} = \begin{pmatrix} \boldsymbol{\Gamma} \tilde{\boldsymbol{\eta}} \\ \boldsymbol{\Theta} \tilde{\boldsymbol{\eta}} \end{pmatrix} = \int_{t_n}^{t_{n+1}} dt e^{\hat{\gamma}(t-t_{n+1})} \begin{pmatrix} \boldsymbol{\eta} \\ \mathbf{0} \end{pmatrix}, \quad (34)$$

$$\begin{aligned} \mathbf{F}_{\text{int}} &= \begin{pmatrix} \boldsymbol{\Gamma} \mathbf{f}_n \\ \boldsymbol{\Theta} \mathbf{f}_n \end{pmatrix} = \int_{t_n}^{t_{n+1}} dt e^{\hat{\gamma}(t-t_{n+1})} \begin{pmatrix} \mathbf{f}_n \\ \mathbf{0} \end{pmatrix} \\ &= \hat{\gamma}^{-1} (\mathbf{I} - e^{-\hat{\gamma}\delta t}) \begin{pmatrix} \mathbf{f}_n \\ \mathbf{0} \end{pmatrix}. \end{aligned} \quad (35)$$

The expressions for $\mathbf{\Lambda}$, $\mathbf{\Gamma}$ and $\mathbf{\Theta}$ matrices are quite complex so they are given in Appendix B. Using this integration scheme, one is in principle able to work with large time steps for the dynamics since all the high frequency vibrations are substantially damped in this type of dynamics. Similarly to the classical case, we can compute the noise correlation matrix by using its definition:

$$\langle \mathbf{E}_{\text{int}}^T \mathbf{E}_{\text{int}} \rangle = \int_{-\delta t}^0 dt e^{\gamma t} \hat{\alpha} e^{\gamma^\dagger t}, \quad (36)$$

where

$$\hat{\alpha} = \begin{pmatrix} \alpha & 0 \\ 0 & 0 \end{pmatrix}. \quad (37)$$

Once again, we refer the reader to the Appendix B for the analytic expression of the noise correlators in the quantum case.

After setting up the general formalism, we need to define the γ matrix in order to fully determine the numerical scheme, as we have done for the classical algorithms (Secs. II A and II B). In the quantum case γ is a $3NM \times 3NM$ matrix. Moreover, we want that $[\mathbf{K}, \gamma] = 0$. Let us first introduce γ^{BO} as a $3N \times 3N$ matrix which is bead independent and defined as in the classical case, namely $\gamma_{ij}^{\text{BO}} = \gamma_{\text{BO}} \delta_{ij}$ for deterministic forces, with γ_{BO} a free parameter, to be optimized. In the case of noisy forces, γ^{BO} will have off-diagonal elements, as we have anticipated for the classical algorithms. This is explained in Sec. III D. Therefore, γ^{BO} should retain all “optimal” damping properties related to the physics of each replica (i), set by the BO force $\mathbf{f}^{(i)}$. We assume that the physics within each replica does not change from one bead to another, thus the optimal γ^{BO} can be taken as bead independent.

The additional complication of the quantum case is represented by the harmonic matrix \mathbf{K} , coupling the beads to each other, whose eigenvalues are $\lambda_k = \omega_k^2$ for $k = 1, \dots, M$, where

$$\omega_k = 2\tilde{\omega}_M \sin\left(\frac{(k-1)\pi}{M}\right) \quad \text{for } k = 1, \dots, M. \quad (38)$$

The energy scale set by \mathbf{K} can be much larger than the one of the BO potential energy surface. In the case the BO forces \mathbf{f} are set to zero, one can compute analytically the relevant autocorrelation time τ_H (using H as operator in Eq. (48)) of the related Langevin dynamics. It has been shown^{69,76} that the optimal damping which minimizes τ_H is given by $\gamma_{\text{harm}}^{(k)} = 2\omega_k$, for each harmonic eigenmode k .

We would like γ to be optimal for both BO and harmonic dynamics. A way to define such a matrix is to exploit the commutator $[\mathbf{K}, \gamma] = 0$, which implies that γ and \mathbf{K} share a common set of eigenvectors. Thus, we can work in a rotated frame which diagonalizes both

γ^{BO} (bead independent) and \mathbf{K} (particle independent). In this frame γ is diagonal, with eigenvalues:

$$\gamma_i^{(k)} = \gamma_i^{\text{BO}} + \gamma_{\text{harm}}^{(k)} \quad (39)$$

for the set of eigenvectors of both γ^{BO} (lower index) and \mathbf{K} (upper index). This uniquely defines the full matrix γ , as it can be reconstructed from its eigenvectors and eigenvalues. For noisy forces the γ_i^{BO} spectrum will be non trivial, while for deterministic forces we have $\gamma_i^{\text{BO}} = \gamma_{\text{BO}} \forall i$. Thus, even in the quantum case which mixes harmonic with physical modes, the only parameter left to tune is γ_{BO} , as the optimal damping for harmonic forces is fully determined by Eq. (38).

To summarize, we have introduced here an algorithm which is able to integrate simultaneously both the physical molecular and the fictitious ring polymer vibration modes in a single time step δt . This could be appealing, but it turns into a disadvantage, as we will see in the tests reported in Sec. II E. Indeed, the compromise between physical and harmonic modes made for the friction in Eq. (39) does not seem optimal. That choice leads to overdamped dynamics with lower diffusion. Moreover, we recall that in Eq. (33) we made the approximation of constant BO forces \mathbf{f} during the time step δt . This condition is hard to meet for fast vibrational modes driven by \mathbf{K} . The resulting algorithm turns out to be less stable as a function of the number of beads M and the time step δt . We are going to improve it, by resorting to a Trotter breakup in order to explicitly separate the harmonic part from the BO one.

D. Trotter breakup and Path Integral Ornstein-Uhlenbeck Dynamics (PIOUD)

The previous PIMPC algorithm can be improved by employing the Liouvillian approach, that is used to integrate the Fokker-Planck differential equation, describing the evolution of the ensemble probability density $\rho(\mathbf{p}, \mathbf{q}, t)$ ⁶³. Since the Fokker-Planck is a linear differential equation, this quantity evolves formally as $\rho(t + \delta t) = e^{-\mathcal{L}\delta t} \rho(t)$, with \mathcal{L} being the Liouville operator, defined as

$$\mathcal{L} = \sum_{i=1}^{3NM} \left(\mathcal{F}_i \partial_{p_i} + p_i \partial_{q_i} - \sum_{j=1}^{3NM} \gamma_{ij} \left(\partial_{p_i} p_j + k_B T M \partial_{p_i} \partial_{p_j} \right) \right) \quad (40)$$

in mass-scaled coordinates. \mathcal{L} is built upon the Hamiltonian propagation, driven by the first two terms, and the Langevin thermostat, represented by the last two, deriving from the Fokker-Planck equation. For the sake of readability, i and j run here over all particles and beads indexed together. In Eq. (40), $\mathcal{F}_i \equiv f_i^{\text{BO}} + f_i^{\text{harm}}$ is the generalized force, comprising the BO and harmonic contributions, i.e. $f_i^{\text{BO}} \equiv f_i = -\partial_{q_i} \tilde{V}$ and $f_i^{\text{harm}} \equiv -\sum_j K_{ij} q_j$, respectively.

As we have seen in Sec. II C, the quantum-to-classical isomorphism Hamiltonian in Eq. (24) includes very different energy scales. For instance, if one works with a large number of beads M , the ring polymer vibration modes can become much stiffer than the molecular vibrations arising from the BO potential. For the PIMPC algorithm, introduced in Sec. II C and tested in Sec. II E, we found that propagating simultaneously all these modes is not optimal since soft modes will be overdamped and the phase space sampling will be less efficient. To overcome this problem, we would like to split the Liouvillian in Eq. (40) into just two operators, one containing only the physical (BO) modes, the other depending exclusively on the fictitious (harmonic) modes. To do so, we first separate the friction matrix into two contributions, in a way analogous to Eq. (39):

$$\gamma = \gamma^{\text{BO}} + \gamma^{\text{harm}}. \quad (41)$$

We can then rewrite the total Liouvillian as the sum of two terms, $\mathcal{L} = \mathcal{L}^{\text{BO}} + \mathcal{L}^{\text{harm}}$, where

$$\mathcal{L}^{\text{harm}} = \sum_i \left(f_i^{\text{harm}} \partial_{p_i} + p_i \partial_{q_i} - \sum_j \gamma_{ij}^{\text{harm}} \left(\partial_{p_i} p_j + k_B T M \partial_{p_i} \partial_{p_j} \right) \right), \quad (42)$$

$$\mathcal{L}^{\text{BO}} = \sum_i \left(f_i^{\text{BO}} \partial_{p_i} - \sum_j \gamma_{ij}^{\text{BO}} \left(\partial_{p_i} p_j + k_B T M \partial_{p_i} \partial_{p_j} \right) \right), \quad (43)$$

in such a way that we can break up the evolution operator via Trotter factorization⁷¹. In order to preserve the reversibility of the process and reduce at most the time step error, we approximate the propagation using a symmetric form^{77,78}:

$$e^{-\mathcal{L}\delta t} \simeq e^{-\mathcal{L}^{\text{BO}}\delta t/2} e^{-\mathcal{L}^{\text{harm}}\delta t} e^{-\mathcal{L}^{\text{BO}}\delta t/2}. \quad (44)$$

The equations of motion corresponding to $\mathcal{L}^{\text{harm}}$ are those in Eq. (13) with the generalized $\hat{\gamma}$ of Eq. (30) where $\mathbf{F} = 0$. They are *linear* in both \mathbf{p} and \mathbf{q} , thus exactly solvable in an analytic closed form. They describe an OUP, and their algebra and properties have been exploited in the GLE framework, where they are used to propagate external auxiliary variables together with the physical momenta in order to generate a colored noise with a corresponding effective memory kernel. In the present algorithm we are going to use the OUP to integrate directly the SDE for both \mathbf{p} and \mathbf{q} , together with the Langevin noise, namely without further splitting the Langevin thermostat in $\mathcal{L}^{\text{harm}}$. The resulting evolution is given by the coupled equations in (33), but with the notable difference of \mathbf{f}_n set to zero, as the BO component of the total force has been loaded in the \mathcal{L}^{BO} Trotter factors. As we mentioned in Sec. II C, dropping

the time dependence of \mathbf{f}_n was the only approximation made in the PIMPC case. Here, there is no time dependence either in \mathbf{f}_n or in γ^{harm} , and thus $e^{-\mathcal{L}^{\text{harm}}\delta t}$ is applied exactly. γ^{harm} is defined as in Sec. II C, namely it is the optimal damping for the dynamics driven by a harmonic H in its normal modes representation. However, in this case there is no low-energy damping for small frequencies in γ^{harm} . Thus, we need to introduce another one, γ_0 , specific to $\mathcal{L}^{\text{harm}}$, such that in the normal modes representation γ^{harm} is diagonal and reads:

$$\gamma_{\text{harm}}^{(k)} = \begin{cases} 2\omega_k & \text{if } 2\omega_k \geq \gamma_0 \\ \gamma_0 & \text{otherwise,} \end{cases} \quad (45)$$

for $k = 1, \dots, M$. In other words, the thermostat controlled by the friction γ_0 is mainly applied to the centroid rototranslational modes which would not be thermalized otherwise because their frequency is zero. Contrary to the other free quantum harmonic modes, the optimal damping γ_0 is not general and has to be optimized for the system under study.

The equation of motion corresponding to \mathcal{L}^{BO} is the one in Eq. (8). Indeed, only the momenta are evolved in \mathcal{L}^{BO} . Therefore, no MPC algorithm is needed, and the resulting equations are similar to those of the simple classical Langevin algorithm introduced in Sec. II A, restricted to \mathbf{p} , which in the present case is a $3NM$ -dimensional vector. The corresponding γ^{BO} is taken block diagonal according to the bead index, and possibly bead dependent. Indeed, there is no need of imposing any commutation relation between γ and \mathbf{K} in this case (for the Trotter decomposition in Eq. (44)), at variance with the PIMPC algorithm of Sec. II C. Thus, every bead can have its own γ^{BO} . On the one hand, this is very useful for QMC noisy forces, as the statistics of the QMC force covariance matrix is genuinely bead dependent, because the wave function is sampled independently for each bead (see Sec. III). In the QMC case, γ^{BO} is fundamental to correct the intrinsic QMC noise affecting the BO forces. On the other hand, for deterministic BO forces, the corresponding γ^{BO} can be taken equal to zero, and Eq. (8) will result in a simple velocity update $\mathbf{p}_{n+1} = \mathbf{p}_n + \frac{\delta t}{2} \mathbf{f}_n$. In fact, any additional damping in the BO modes will turn into a slower algorithmic diffusion, as the thermalization is already guaranteed by the Langevin thermostat integrated in $\mathcal{L}^{\text{harm}}$. In this limit, \mathcal{L}^{BO} will reduce to \mathcal{L}_V , using the same notations as in Ref. 69.

For deterministic forces, Ceriotti and coworkers⁶⁹ developed a different algorithm (dubbed PILE), where the main difference with respect to ours is that $\mathcal{L}^{\text{harm}}$ is split into \mathcal{L}_0 , which propagates the motion of the harmonic oscillators in their normal modes representation, and \mathcal{L}_γ (the part proportional to $\gamma_{ij}^{\text{harm}}$ in Eq. (42), \mathcal{L}_0 being the remaining part in the first line of the same equation), which corresponds to the Langevin thermostat acting on the normal modes. The total Liouvillian propagator proposed in Ref. 69 is:

$$e^{-\mathcal{L}\delta t} \simeq e^{-\mathcal{L}_\gamma\delta t/2} e^{-\mathcal{L}_V\delta t/2} e^{-\mathcal{L}_0\delta t} e^{-\mathcal{L}_V\delta t/2} e^{-\mathcal{L}_\gamma\delta t/2}. \quad (46)$$

Apart from the additional Trotter breakup, in the above sequence of operators the Langevin thermostat on the normal modes is the outermost part of the Liouvillian decomposition, for a better control of the target temperature. Our algorithm in Eq. (44) performs better than the solution proposed in Eq. (46), since in our case $\mathcal{L}^{\text{harm}} = \mathcal{L}_0 + \mathcal{L}_\gamma$ corresponds to an exact propagator including both the coordinates change and the thermalization of the free quantum ring polymer after having applied a normal modes transformation. As a consequence, one Trotter factorization is saved which in principle enables us to work with a larger time step δt or more quantum replicas M . Indeed, the Trotter break-up is obviously exact if the two operators involved commute. The split of $\mathcal{L}^{\text{harm}}$ proposed by Ceriotti is a very unfortunate choice as the commutator of $[\mathcal{L}_0, \mathcal{L}_\gamma]$ is dominated by the term $\gamma_{ij}^{\text{harm}} f_j^{\text{harm}} \partial_{p_i}$ which is diverging as M^3 for large M , as it can be easily seen by the exact expression of the harmonic forces and the choice of the optimal friction. This argument suggests that our method, involving commutators at most diverging as M^2 , should have a time step error much better behaved for large M .

These algorithmic improvements will be tested and discussed in the next section.

E. Algorithm stability with deterministic forces

We test the robustness of the three different algorithms (PIMPC, PILE and PIOUS) detailed in Sec. II C and II D by performing PILD simulations on the Zundel ion with almost exact deterministic forces which are simply computed by finite differences of the CCSD(T) PES provided by Huang and coworkers⁵³. Since our only aim here is to test the different integration schemes, the number of MD iterations $N_{\text{iter}} = 100000$ is quite small to visit the entire phase space but sufficient to identify some possible weakness of the propagators. We recall that PIMPC denotes the propagator corresponding to the Eq. (33) since positions and velocities evolve jointly, whereas the PIOUS integrator corresponds to Eq. (44), in which we separate the physical from the fictitious vibration modes of the system.

These algorithms will be compared to the very efficient PILE integrator of Eq. (46). An efficient PILD algorithm must be stable with both large time step and large number of quantum replicas. Indeed, the collective modes of a large ring polymer become very stiff, so much more difficult to control, especially if the integration time step is large. A correct average temperature and close values of the virial and the primitive estimators, given in Eq. (28) and (29) respectively, point that we are sampling properly both the positions and the momenta of all particles.

Beside temperature and kinetic energy, other observables will also be used here to quantify the numerical efficiency of the tested algorithms. A very stable propagation of the equations of motion can for instance be due to an overcautious (too small δt) integration of the

dynamics, which does not constitute a real improvement since the phase space will be poorly visited. To this purpose, Ceperley introduced the algorithmic diffusion constant D which reads as⁷⁹

$$D = \left\langle \frac{\left[\tau \sum_{i=1}^{3N} \sum_{j=1}^M \left(q_i^{(j)}(t + \delta t) - q_i^{(j)}(t) \right) \right]^2}{T_{\text{iter}}} \right\rangle. \quad (47)$$

T_{iter} is the total amount of CPU time spent for one single MD iteration at a given time step δt . Since T_{iter} is almost equal for the three algorithms under study, the algorithmic diffusion can be interpreted as the usual diffusion of quantum particles in the position space. Furthermore, we will also focus our attention on the potential autocorrelation time known to be very sensitive to Langevin damping since the softest vibration modes are sometimes very long to sample. This useful quantity has the following expression

$$\tau_V = \frac{1}{\langle V^2 \rangle - \langle V \rangle^2} \int_0^{N_{\text{iter}} \delta t} dt \langle \delta V(0) \delta V(t) \rangle, \quad (48)$$

with $\delta V = V - \langle V \rangle$ the fluctuation of the potential energy. τ_V needs to be minimized to obtain an optimal production run and this is achieved by working with the largest possible time step δt . Simultaneously, an optimal centroid damping γ_0 has to be found to minimize τ_V , as we shall detail later.

1. Stability with respect to the number of beads M

We report here the results obtained for the three different integration schemes (PIMPC, PILE and PIOUS) at low temperature ($T = 50$ K) in Figure 1 and at room temperature ($T = 300$ K) in Figure 2 as a function of the number of quantum replicas M . In each case, the four key observables (virial versus primitive kinetic energy, average temperature, algorithmic diffusion constant and potential autocorrelation time) described in the previous section are compared. We have decided to perform simulations working with an increasing number of beads $M = 4, 8, 16, 32, 64, 128$ and 256, using a reasonable but not-so-small time step $\delta t = 0.5$ fs.

The quantum kinetic energy estimators are known to be useful tools to determine the number of beads required at a given temperature to capture all NQE during the dynamics. However, other quantities such as the algorithmic diffusion constant and the potential autocorrelation time can also be used to diagnose the good convergence of the quantum kinetic energy. Indeed, these observables keep increasing (quantum kinetic energy and diffusion) or decreasing (potential autocorrelation time) when the number of beads increases until they reach a plateau value. In the case of the Zundel ion, $M = 128$ quantum replicas seem to be enough to fully recover the

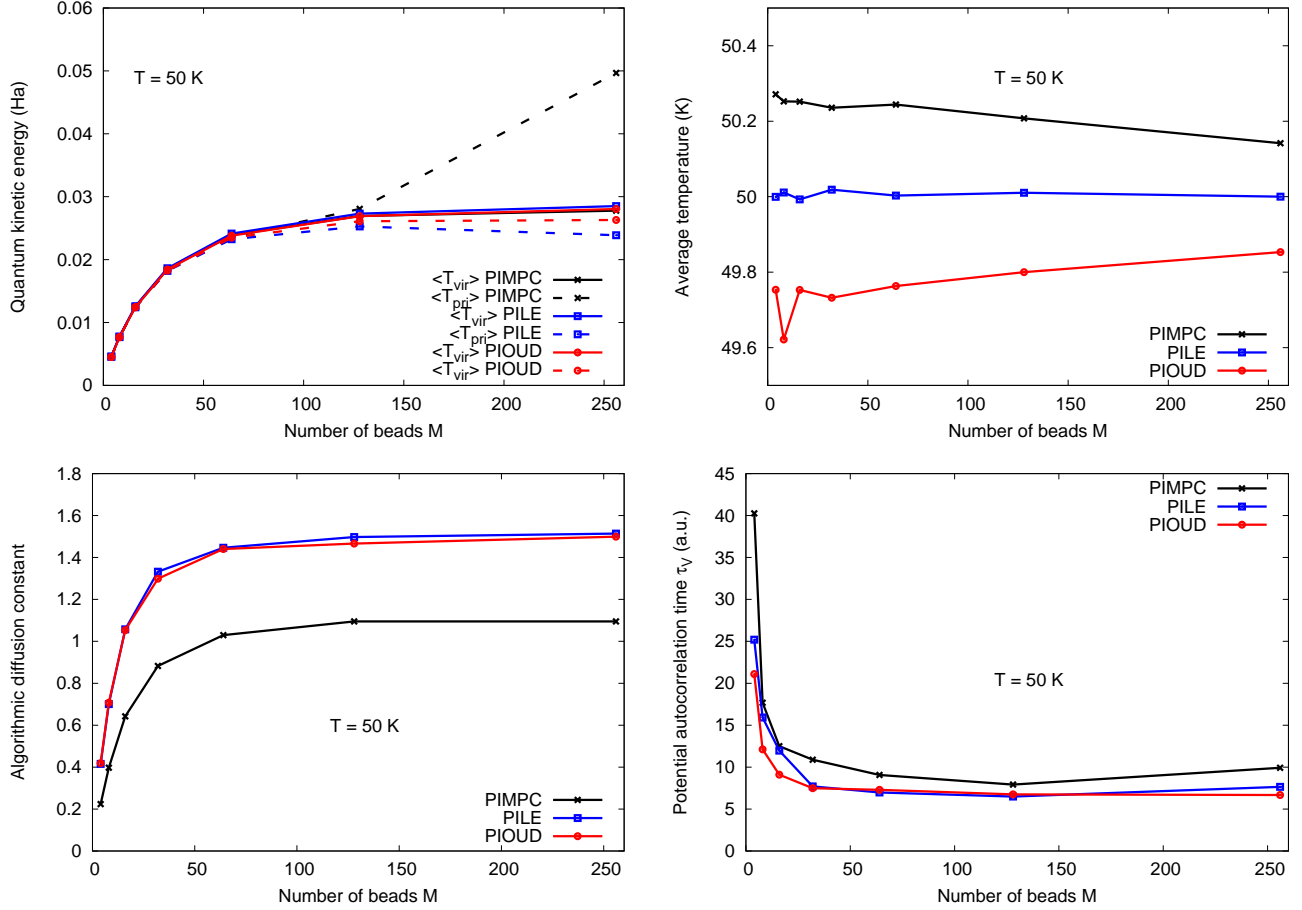


FIG. 1. Evolution of the quantum kinetic energy estimators $\langle T_{\text{vir/pri}} \rangle$ (top left panel), the temperature T (top right panel), the algorithmic diffusion constant D (bottom left panel) and the potential autocorrelation time τ_V (bottom right panel) as a function of the number of quantum replicas M evolving at $T = 50$ K. Solid lines correspond to the virial estimator of the kinetic energy whereas the primitive estimator curves are dashed. Each algorithm has its own color code: black for the PIMPC algorithm, blue for the PILE propagator and red for the PIOUD algorithm. The time step and the friction are respectively set to $\delta t = 0.5$ fs and $\gamma_0 = 1.46 \cdot 10^{-3}$ a.u. (γ_{BO} for the PIMPC algorithm).

quantum kinetic energy at low temperature (see Figure 1), whereas only $M = 32$ beads are required at room temperature according to Figure 2. We note that these values are consistent with those frequently used in the literature for this system^{80–82}.

A rapid inspection of Figures 1 and 2 shows that the PIMPC approach, in which all operations are propagated into one single block without any mode separation during the dynamics, is by far less efficient and stable than the other two. Indeed, the primitive energy estimator becomes unstable for $M = 256$ at 50 K and for $M \geq 32$ at room temperature, showing that this algorithm is not able to handle the stiffest vibration modes of the ring polymer. The asymptotic value of the algorithmic diffusion constant is also dramatically reduced and even slightly decreases at room temperature for very large number of quantum replicas.

Indeed, by working in a mixed space where all the physical and fictitious vibration modes are propagated dur-

ing a single iteration, one has to deal with very different energy scales, spanning various orders of magnitude. This leads to an overdamping of the softest intermolecular modes which are strongly penalized because of the presence of very high frequency modes. This also explains why the potential autocorrelation time is slightly larger for this algorithm while the simulation temperature seems to be rather well-controlled.

The performances of the PIOUD propagator of Eq. (44) and the PILE algorithm are much closer to each other. Looking at the algorithmic diffusion constant and the potential autocorrelation time, the PILE and PIOUD algorithms have the same computational efficiency. This is expected because the same normal mode transformation is applied in both approaches.

PILE exhibits a built-in stability of the average simulation temperature with respect to the number of beads. On the contrary, our algorithms (both PIMPC and PIOUD) display a natural and small time step error on the

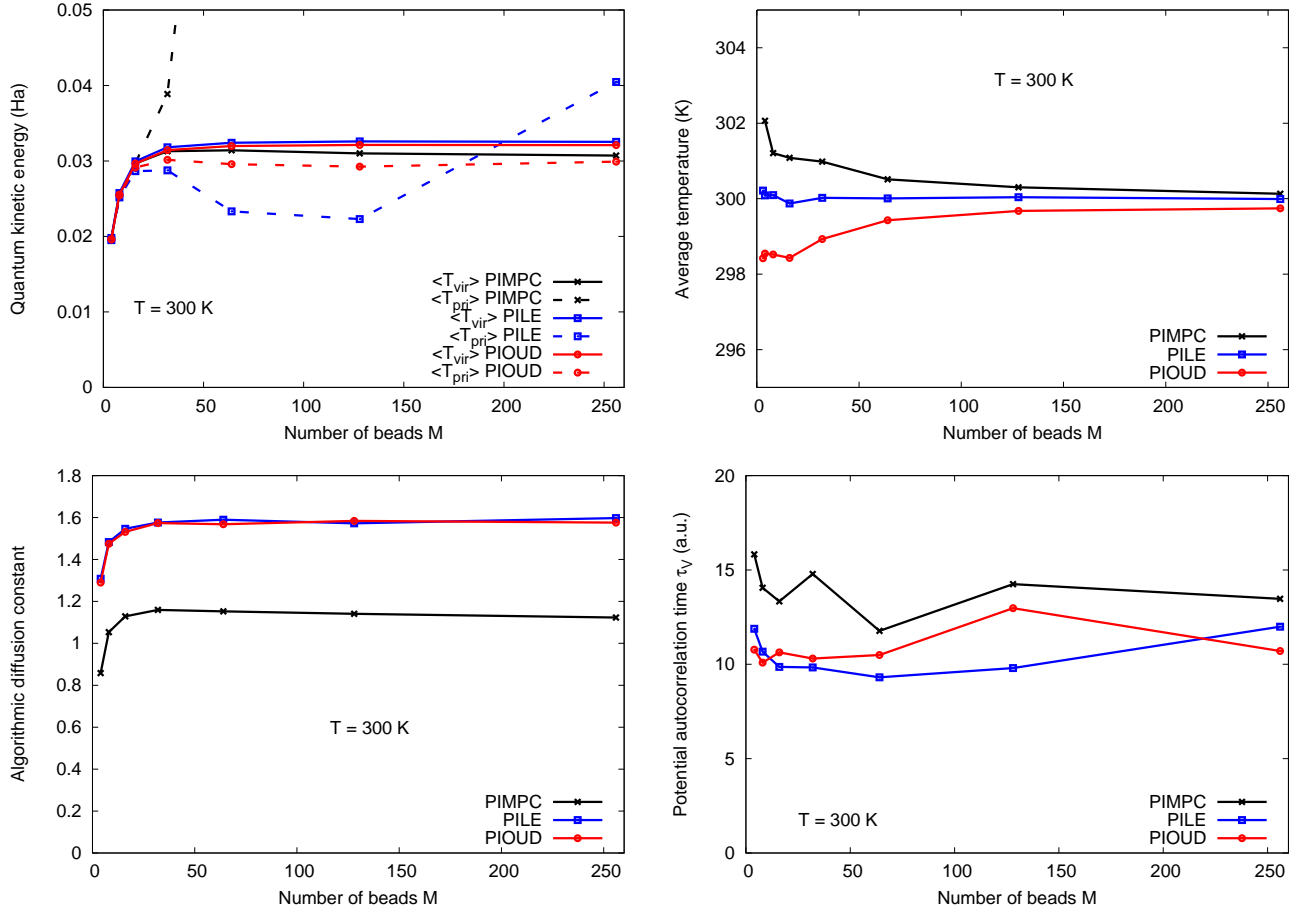


FIG. 2. Evolution of the quantum kinetic energy estimators $\langle T_{\text{vir/pri}} \rangle$ (top left panel), the temperature T (top right panel), the algorithmic diffusion constant D (bottom left panel) and the potential autocorrelation time τ_V (bottom right panel) as a function of the number of quantum replicas M evolving at $T = 300$ K. Solid lines correspond to the virial estimator of the kinetic energy whereas the primitive estimator curves are dashed. Each algorithm has its own color code: black for the PIMPC algorithm, blue for the PILE propagator and red for the PIOUD algorithm. The time step and the friction are respectively set to $\delta t = 0.5$ fs and $\gamma_0 = 1.46 \cdot 10^{-3}$ a.u. (γ_{BO} for the PIMPC algorithm).

target temperature which tends to vanish when the number of beads increases. This temperature difference can be easily explained by the fact the instantaneous velocities (and so the temperature) are measured just after the thermalization step \mathcal{L}_γ in the PILE integration scheme whereas they are evaluated after the \mathcal{L}^{BO} operator in our propagations. Since \mathcal{L}^{BO} includes the propagation according to the ionic forces, that are not harmonic, it is reasonable to expect a larger error in this case. We remark however that an artificially small error in the target temperature is not at all important, because the temperature depends only on the velocities that have a trivial (i.e. Boltzmann) distribution. It is much more important to have the correct distribution for the coordinates q , regardless what is the distribution of the velocities. Nevertheless, when one increases the number of beads, the error made on the target temperature (which is already less than 1%) decreases. Indeed, for large M , the propagation driven by $\mathcal{L}^{\text{harm}}$ becomes dominant over the

BO forces. This implies a more effective control of the temperature because $\mathcal{L}^{\text{harm}}$ corresponds to an exact integration.

When looking at the top left panels of Figures 1 and 2, we notice that the PIOUD algorithm displays an almost perfect control of the kinetic energy operators at each temperature. On the contrary, the PILE algorithm exhibits a significant instability of the primitive energy for a large number of beads ($M \geq 64$) at room temperature. The contrast between the perfect average temperature and the quantum kinetic energy instabilities demonstrates that a good control of the velocities does not necessarily imply an accurate sampling of the positions. The robustness of our approach mainly relies on a simultaneous control of both positions and velocities during the dynamics via momentum-position correlation matrices.

In summary, the PIOUD propagator seems to be more efficient than PILE as the positions are better controlled, which enables us to work with a larger number of quan-

tum replicas at a fixed time step δt .

2. Stability with respect to the time step δt

Thanks to the preliminary analysis discussed in Sec. II E 1, we know how many quantum replicas should be used to generate an efficient and converged PILD simulation of the Zundel ion at a given temperature. Moreover, stability for rather large time steps is crucial in the perspective of performing PILD calculations on larger systems using a PES evaluated by accurate but computationally demanding *ab initio* methods. We performed here CC-PILD simulations at low temperature ($T = 50$ K) with $M = 128$ replicas and at room temperature ($T = 300$ K) with $M = 32$ beads using different values of $\delta t = 0.1, 0.2, 0.3, 0.5, 0.75$ and 1 fs. The behavior of the observables used to evaluate the algorithm efficiency are plotted in Figures 3 and 4 as a function of the time step at 50 K and 300 K, respectively.

Similarly to the previous figures, the PILE propagator exhibits a remarkably stable average temperature when one increases the time step. On the contrary, our PIMPC and PIOUD algorithms are suffering from a time step error arising from the Trotter factorization in the propagation of the equations of motion. In the PILE algorithm instead, the temperature is measured just after the \mathcal{L}_γ step so it is not contaminated by the time step error yet.

To have a clearer idea of the bias induced by the time step error, we check the difference $|\langle T \rangle_{M,\text{vir}} - \langle T \rangle_{M,\text{pri}}|$ which gives us direct information on the accuracy of the positions sampling. Like in the previous tests, the PIOUD algorithm shows the smallest difference thanks to a good control of the primitive energy, due to the separation of the Liouvillian in physical and harmonic modes. The difference between these two kinetic energy estimators is more spectacular at room temperature. Indeed, the fluctuation-dissipation contributions in $\mathcal{L}^{\text{harm}}$, related to damping and random forces in the dynamics, become more important as the temperature increases, while the BO forces are not so strongly affected by thermal effects.

The diffusion constant shows a very similar behavior as a function of time step for the PILE and the PIOUD propagators. As expected, the potential autocorrelation time decreases significantly with increasing the time step without relevant differences between the PILE and the PIOUD algorithms.

The algorithmic tests carried out here have been applied to a deterministic PES and exact analytic forces. We now wish to go further by applying the previous formalism to the case of stochastic PES and forces, such as the ones computed in a QMC framework, without losing computational efficiency.

III. EXTENSION TO THE STOCHASTIC CASE: CORRELATING THE NOISE BY QMC

A. QMC-BO surface and electron wave function

After checking the performances of the integrators with deterministic forces, we shall show that the PIOUD algorithm can be easily extended to perform PILD simulations in a potential energy landscape $V(\mathbf{q})$ evaluated by VMC, namely:

$$V(\mathbf{q}) = \frac{\langle \Psi_{\mathbf{q}} | H(\mathbf{q}) | \Psi_{\mathbf{q}} \rangle}{\langle \Psi_{\mathbf{q}} | \Psi_{\mathbf{q}} \rangle}, \quad (49)$$

where $|\Psi_{\mathbf{q}}\rangle$ is the QMC wave function, that minimizes the expectation value of $H(\mathbf{q})$. In the QMC framework, the evaluation of $V(\mathbf{q})$ and its corresponding force estimators are intrinsically noisy. In Eq. (49) and in the following, we use the \mathbf{q} subscript to make apparent that the VMC wave function has an explicit dependence on the nuclear coordinates. Using the BO approximation, the PES corresponds to the expectation value of the exact Hamiltonian applied to the wave function $|\Psi_{\mathbf{q}}\rangle$ written here as a Jastrow Antisymmetrized Geminal Power (JAGP) product⁸³

$$\Psi_{\mathbf{q}}(\mathbf{x}_1, \dots, \mathbf{x}_{N_{\text{el}}}) = J_{\mathbf{q}}(\mathbf{r}_1, \dots, \mathbf{r}_{N_{\text{el}}}) \Psi_{AGP, \mathbf{q}}(\mathbf{x}_1, \dots, \mathbf{x}_{N_{\text{el}}}). \quad (50)$$

The set $\{\mathbf{x}_i = (\mathbf{r}_i, \sigma_i)\}_{i=1, \dots, N_{\text{el}}}$ represents spatial and spin coordinates of the N_{el} electrons.

On the one hand, the bosonic Jastrow factor $J_{\mathbf{q}}$ is a function of electron-electron separation and mainly describes dynamical correlations due to charge fluctuations and Van der Waals effects. It is often written as a product of one-body, two-body and three/four-body terms $J_{\mathbf{q}} = J_{1, \mathbf{q}} J_{2, \mathbf{q}} J_{3, \mathbf{q}}$. The one body term reads

$$J_{1, \mathbf{q}} = \exp \left(- \sum_i^{N_{\text{el}}} \sum_j^N (2Z_j)^{3/4} u((2Z_j)^{1/4} |\mathbf{r}_i - \mathbf{q}_j|) \right) \quad (51)$$

with $u(|\mathbf{r} - \mathbf{q}|) = \frac{1 - e^{-b|\mathbf{r} - \mathbf{q}|}}{2b}$ and b is a variational parameter. This form is chosen to satisfy the electron-ion Kato cusp conditions, used to deal appropriately with the diverging electron-nucleus Coulomb potentials at short distances. In the Zundel ion Hamiltonian, our benchmark system, we keep the bare Coulomb potential only for hydrogen, while for the oxygen atoms we replace it with the Burkatzki-Filippi-Dolg (BFD) pseudopotential⁸⁴, which is smooth at the electron-ion coalescence points. Thus, $J_{1, \mathbf{q}}$ is applied only to the hydrogen atom. Similarly, the electron-electron cusp conditions are dealt with by the two-body Jastrow factor

$$J_{2, \mathbf{q}} = \exp \left(\sum_{i < j}^{N_{\text{el}}} u(|\mathbf{r}_i - \mathbf{r}_j|) \right), \quad (52)$$

where u is a function of the same form as in Eq. (51), but with a different variational parameter. Finally, many-body correlations are included in the remaining part of

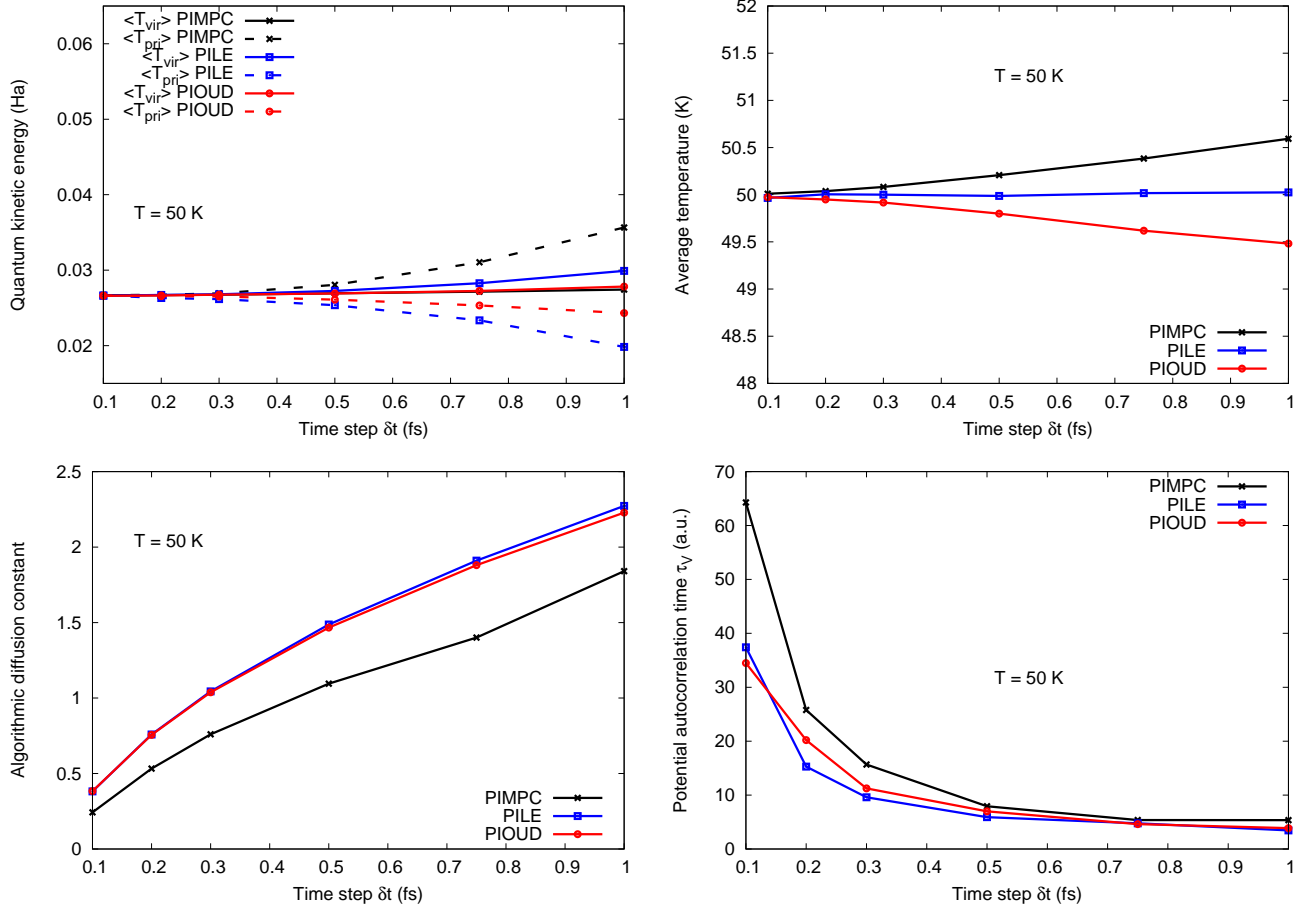


FIG. 3. Evolution of the quantum kinetic energy estimators $\langle T_{\text{vir/pri}} \rangle$ (top left panel), the temperature T (top right panel), the algorithmic diffusion constant D (bottom left panel) and the potential autocorrelation time τ_V (bottom right panel) as a function of the time step δt at $T = 50$ K. Solid lines correspond to the virial estimator of the kinetic energy whereas the primitive estimator curves are dashed. Each algorithm has its own color code: black for the PIMPC algorithm, blue for the PILE propagator and red for the PIOUD algorithm. $M = 128$ quantum replicas are used and the friction is set to $\gamma_0 = 1.46 \cdot 10^{-3}$ a.u. (γ_{BO} for the PIMPC algorithm).

the Jastrow factor

$$J_{3,\mathbf{q}} = \exp \left(\sum_{i < j}^{N_{\text{el}}} \Phi_{J_{\mathbf{q}}}(\mathbf{r}_i, \mathbf{r}_j) \right), \quad (53)$$

with

$$\Phi_{J_{\mathbf{q}}}(\mathbf{r}_i, \mathbf{r}_j) = \sum_{a,b}^N \sum_{\mu,\nu}^{N_{\text{basis}}} g_{\mu,\nu}^{a,b} \Psi_{a,\mu}^J(\mathbf{r}_i - \mathbf{q}_a) \Psi_{b,\nu}^J(\mathbf{r}_j - \mathbf{q}_b), \quad (54)$$

where N_{basis} is the number of $\Psi_{a,\mu}^J$, the Gaussian Type Orbitals (GTOs) constituting the primitive basis of each atom a . The Jastrow functional form has been developed on a primitive Gaussian basis set of O(3s,2p,1d) H(2s,1p) corresponding to 213 Jastrow parameters.

On the other hand, since our system is spin unpolarized, the Fermionic part of the wave function is expressed as an antisymmetrized product of the geminals or pairing

(AGP) functions $\Phi_{\mathbf{q}}(\mathbf{x}_i, \mathbf{x}_j)$:

$$\Psi_{AGP,\mathbf{q}}(\mathbf{x}_1, \dots, \mathbf{x}_{N_{\text{el}}}) = \hat{A} [\Phi_{\mathbf{q}}(\mathbf{x}_1, \mathbf{x}_2), \dots, \Phi_{\mathbf{q}}(\mathbf{x}_{N_{\text{el}}-1}, \mathbf{x}_{N_{\text{el}}})]. \quad (55)$$

The geminals are antisymmetric functions of two electron coordinates written as a product of a spatial symmetric part and a spin singlet

$$\Phi_{\mathbf{q}}(\mathbf{x}_i, \mathbf{x}_j) = \phi_{\mathbf{q}}(\mathbf{r}_i, \mathbf{r}_j) \frac{\delta(\sigma_i, \uparrow) \delta(\sigma_j, \downarrow) - \delta(\sigma_i, \downarrow) \delta(\sigma_j, \uparrow)}{\sqrt{2}}, \quad (56)$$

where the $\phi_{\mathbf{q}}(\mathbf{r}_i, \mathbf{r}_j)$ can be expanded either over the size-reduced primitive basis (O(5s5p2d) and H(4s2p) for the determinantal part) or the computationally more efficient hybrid orbitals $\bar{\Psi}^{AGP}$, also developed on GTOs, such that

$$\phi_{\mathbf{q}}(\mathbf{r}_i, \mathbf{r}_j) = \sum_{a,b}^N \sum_{\mu,\nu}^{N_{\text{hyb}}} \lambda_{\mu,\nu}^{a,b} \bar{\Psi}_{a,\mu}^{AGP}(\mathbf{r}_i - \mathbf{q}_a) \bar{\Psi}_{b,\nu}^{AGP}(\mathbf{r}_j - \mathbf{q}_b). \quad (57)$$

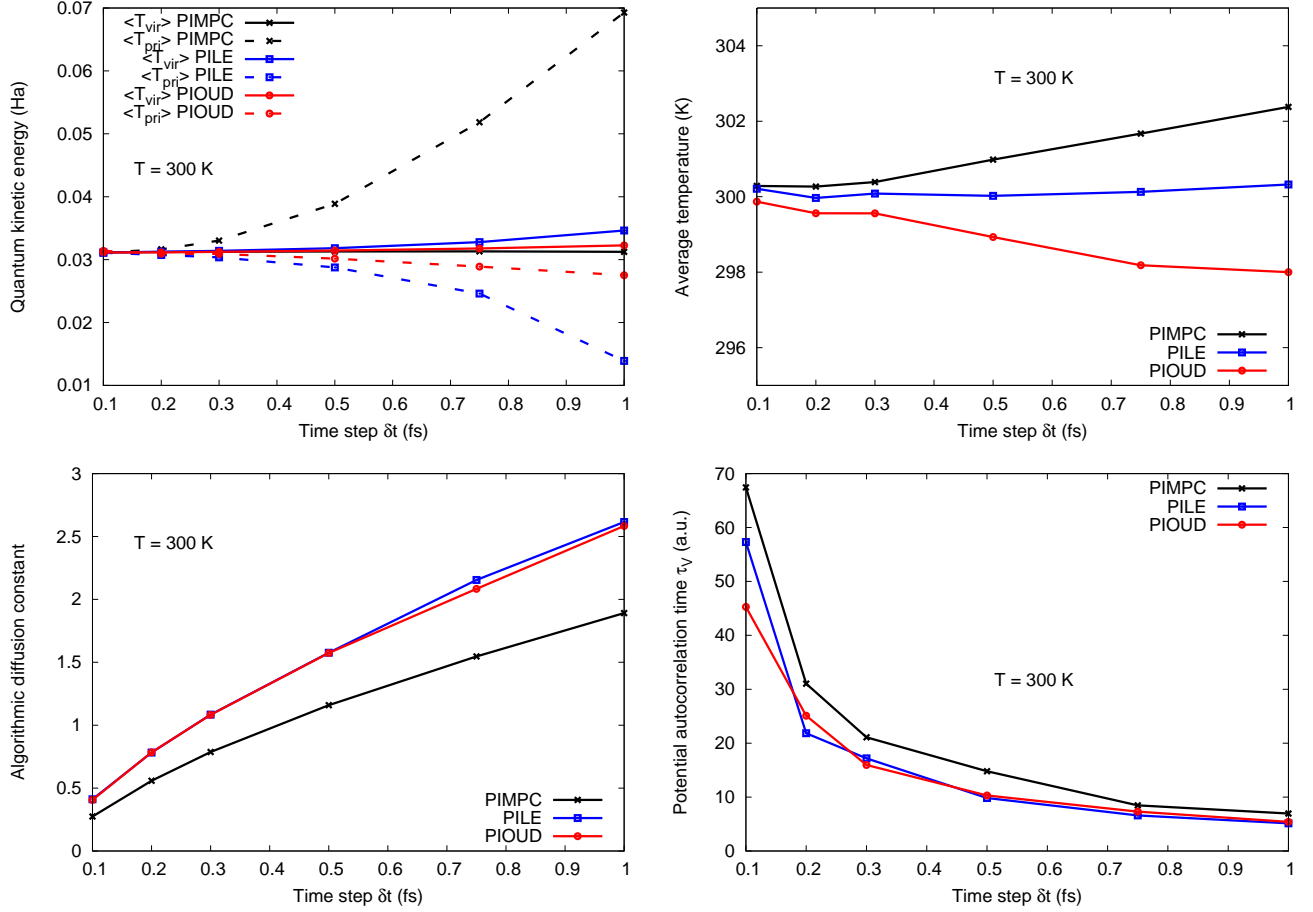


FIG. 4. Evolution of the quantum kinetic energy estimators $\langle T_{\text{vir/pri}} \rangle$ (top left panel), the temperature T (top right panel), the algorithmic diffusion constant D (bottom left panel) and the potential autocorrelation time τ_V (bottom right panel) as a function of the time step δt at $T = 300$ K. Solid lines correspond to the virial estimator of the kinetic energy whereas the primitive estimator curves are dashed. Each algorithm has its own color code: black for the PIMPC algorithm, blue for the PILE propagator and red for the PIOUD algorithm. $M = 32$ quantum replicas are used and the friction is set to $\gamma_0 = 1.46 \cdot 10^{-3}$ a.u. (γ_{BO} for the PIMPC algorithm).

Indeed, one can apply here the geminal embedding scheme⁸⁵ to obtain $N_{\text{hyb}} < N_{\text{basis}}$ geminal embedding orbitals (GEOs), to reduce the total number of parameters, that is almost proportional to the computational cost dedicated to the optimization of the wave function. Here, we use the 80 2H hybrid basis set which has been proven to be the best compromise between accuracy and computational cost, due to a limited number (571) parameters describing the determinantal part of the wave function⁸⁶. This point is very important, because in the present optimization methods^{83,87,88}, the matrices involved in the iterative procedure have linear dimension equal to the number p of parameters involved. The number of QMC sampling used to characterize stochastically a $p \times p$ matrix should be much larger than p , otherwise the matrix is biased if not rank deficient, and the QMC optimization methods no longer work. Thus, it is clear that the reduction of the number of parameters is very much needed at present, because it is basically proportional to the com-

putational cost of QMC optimization.

In this paper we use the optimal wave function devised by Dagrada *et al.* for the same system at zero temperature; all the technical details concerning the variational wave function can be found in Ref. 86.

During the dynamics, the GTO exponents in both the Jastrow and the AGP part of the wave function are kept frozen to make the simulation stable. At each new ionic configuration, the wave function must be reoptimized. This is done by means of the Stochastic Reconfiguration (SR)^{83,87}, or the optimization method with Hessian acceleration (SRH)⁸⁸. As the ionic positions are smoothly connected to those of the previous MD time step, also the wave function parameters will evolve continuously. After each nuclear iteration, the wave function is optimized by few (five in our simulations of the Zundel ion) SR or SRH steps on the electronic parameters to ensure that the system is close enough to the BO surface, before continuing the propagation of the ion dynamics. Due to

the continuity of the nuclear trajectories, the number of SR steps is significantly smaller than the one required for a wave function optimization from scratch.

B. Bead-grouping approximation

Another advantage of our framework is represented by the local, ion-centered, basis set. We start from the observation that the most relevant dependence of the wave function on the ionic positions \mathbf{q} comes directly (and explicitly) from the basis set, while the dependence of the electronic variational parameters is generally weaker. This is particularly true in quantum MD calculations, where each particle is represented by an M -bead necklace. In the first approximation, a necklace could share the same wave function parameters, while the full \mathbf{q} dependence is provided by the basis set only, a dependence coming from the atomic centers -different in each bead- defining the basis set at each different time slice. This approximation can be very effective to reduce the computational burden, because the main drawback encountered in PIMD and PILD calculations with respect to their classical counterparts is the factor-of- M increase of variational parameters involved ($M \times p$ if no approximation is employed). Conversely, if the number of variational parameters is restricted to the same number as the classical simulation, no computational overhead is expected to work with $M > 1$ in QMC. Indeed, the evaluation of the ionic forces can be done with a number of samples inversely proportional to M , as the temperature in each time slice is increased by M and the Langevin equations require statistically less accurate -but nevertheless unbiased- forces, so that the M evaluations of forces at each time slice are essentially cost-free in QMC³³.

When instead forces are computed with deterministic methods - e.g. DFT- the computational burden is necessarily proportional to M , and therefore several techniques have been recently developed to decrease the number of evaluations of the ionic forces by about an order of magnitude without missing any significant NQE. This is done by achieving smart interpolations and groupings of the different possible paths^{89,90} or by applying a Ring Polymer Contraction (RPC) scheme⁹¹⁻⁹³. Otherwise, the number of quantum replicas can be reduced by working with a GLE including a colored noise mimicking the quantum fluctuations of the nuclei^{55,67,75,94}.

Although these methods could be effectively incorporated into our QMC framework, we are forced to explore another approach, because, as we have discussed, in QMC the problem is just the large number of variational parameters, and not the large value of M . We introduce therefore a method which takes advantage of the explicit wave function representation of the electronic problem. Indeed, each bead at each iteration has its own optimal wave function $|\Psi_{\mathbf{q}}^{(k)}\rangle$, for $k = 1, \dots, M$, which minimizes the variational energy at the nuclear configuration $\mathbf{q}^{(k)}$. Consequently, we need to find the best variational pa-

rameters set $\boldsymbol{\lambda}^{(k)} = \{g_{\mu,\nu}^{a(k),b(k)}, \lambda_{\mu,\nu}^{a(k),b(k)}, b^{(k)}\}$, orbital contraction coefficients, ... for each wave function. Despite the availability of efficient QMC optimization algorithms, that task is still computationally demanding and would limit the application of our method to very small systems. To overcome this major difficulty, we exploit the local nature of the Gaussian basis sets used in the expansion of both the Jastrow and AGP factors. As anticipated, we make the approximation of defining N_{groups} groups of neighboring beads and constraining the wave function parameters to be equal for all beads in the same group. Since a group shares the same parameters, the corresponding energy gradients are then averaged over the quantum replicas constituting the group. In this way, we improve the statistics by a factor of M/N_{groups} . We obtain less noisy parameters even though the resulting wave function is not exactly optimized for each quantum replica. We mention that this is a controllable and systematically improvable approximation. Indeed, if one takes $N_{\text{groups}} = M$, the electronic result is exact, whereas $N_{\text{groups}} = 1$ constitutes the roughest approximation. In the latter case, one performs a fully quantum dynamics with almost the same statistics as the one with classical nuclei. We are going to test and validate this approximation for the Zundel ion (see Sec. IV). In the case of the simple hydrogen molecule the approximation with $N_{\text{groups}} = 1$ allows one to recover 90% of the Zero Point Energy (ZPE).

C. QMC ionic forces

Performing MD and PIMD simulations with a QMC-generated PES relies on the possibility of evaluating the nuclear forces with finite variance and in a reasonable amount of time. As already done in the previous sections, we denote the $3NM$ -dimensional force acting on all the NM quantum replicas by

$$\mathbf{f} = -\nabla_{\mathbf{q}} V(\mathbf{q}) \quad (58)$$

where $\nabla_{\mathbf{q}}$ is the gradient relative to the Cartesian coordinates \mathbf{q} of all the images of the nuclei. By taking into account all the implicit and explicit dependence of $V(\mathbf{q})$ on both the nuclear positions \mathbf{q} and the electronic parameters set $\boldsymbol{\lambda}$, Eq. (58) can be decomposed into three different contributions:

$$\mathbf{f} = \mathbf{f}^{\text{HF}} + \mathbf{f}^{\text{Pulay}} + \mathbf{f}^{\boldsymbol{\lambda}}, \quad (59)$$

with

$$\begin{aligned} \mathbf{f}^{\text{HF}} &= -\frac{\langle \Psi | \nabla_{\mathbf{q}} H | \Psi \rangle}{\langle \Psi | \Psi \rangle}, \\ \mathbf{f}^{\text{Pulay}} &= -2 \frac{\langle \Psi | O_{\mathbf{q}} H | \Psi \rangle - \langle \Psi | O_{\mathbf{q}} | \Psi \rangle V}{\langle \Psi | \Psi \rangle}; \quad O_{\mathbf{q}} | \Psi \rangle = \nabla_{\mathbf{q}} | \Psi \rangle, \\ \mathbf{f}^{\boldsymbol{\lambda}} &= \nabla_{\boldsymbol{\lambda}} V \cdot \nabla_{\mathbf{q}} \boldsymbol{\lambda}. \end{aligned} \quad (60)$$

In principle, the term $\mathbf{f}^{\boldsymbol{\lambda}}$ is the most complicated because the derivatives $\nabla_{\mathbf{q}} \boldsymbol{\lambda}$ are very difficult to evaluate. Fortunately, this contribution cancels out when the set of

electronic parameters λ is fully optimized, as the energy of the system becomes minimal. The Hellmann-Feynman (HF) term \mathbf{f}^{HF} is the only contribution which would survive if the HF theorem were applicable. This is not the case, because the wave function is not an eigenstate of H . Nevertheless, when the wave function approaches an eigenstate of H , the Pulay term gets smaller and the HF term becomes dominant.

Computing the HF and Pulay terms with finite variance and in a fast way is of paramount importance to make a QMC-based MD and PIMD possible. Some improvements, such as the correlated sampling (CS) and the space warp coordinate transformation (SWCT)⁹⁵, have been done. A further step in the evaluation of efficient and accurate forces is the algorithmic differentiation (AD), recently introduced by Sorella and Capriotti⁹⁶. Thanks to the AD, computing all components of the ionic forces is only four times more expensive than the cost of an energy calculation. By employing all the techniques described above, we are able to evaluate \mathbf{f} in an affordable computational cost with increasing system size.

D. QMC noise correction

In our approach, the potential energy landscape and thus the ionic forces acting on each particles are evaluated by VMC. Consequently, a statistical noise due to the stochastic nature of this method is introduced, and must be kept under control if we want to have an unbiased sampling of the phase space during the dynamics. Fortunately, the methodology described in the previous sections is particularly suited for this situation, as it deals with the most general case, where the friction γ and covariance α matrices are not diagonal. This corresponds to the inclusion of a correlated noise into the dynamics, in contrast to the more usual white noise case. By construction, we can now make the assumption that there exists also a QMC contribution to the covariance matrix which becomes position-time dependent³⁴

$$\alpha(\mathbf{q}) = \alpha_{\text{BO}} \mathbf{I} + \Delta_0 \alpha^{\text{QMC}}(\mathbf{q}). \quad (61)$$

$\alpha_{\text{BO}} = 2k_B T \gamma_{\text{BO}}$ is the white noise contribution and Δ_0 is a tunable parameter which is mainly set to make the covariance (and thus the friction) matrix positive definite. α and γ are linked by the FDT, while α^{QMC} is the QMC-force covariance matrix defined by

$$\alpha_{ij}^{\text{QMC}} = \langle \delta f_i \delta f_j \rangle, \quad (62)$$

where $\delta f_i = f_i - \langle f_i \rangle$ is the fluctuation of the i -th ionic force. Previous works have established that the QMC covariance matrix is roughly proportional to the dynamical matrix (it is exactly proportional for harmonic forces). Therefore, it carries information on the vibrational properties of the system⁹⁷. As a consequence, one could take advantage of an apparent drawback of the QMC

approach by using the intrinsic noise to drive a dynamics in the phase space with nearly optimal sampling.

However, to fulfill the FDT, the QMC noise has to be disentangled from the total Langevin noise in the following way:

$$\eta_i = \eta_i^{\text{ext}} + \eta_i^{\text{QMC}} \quad (63)$$

such that $\alpha_{ij}^{\text{QMC}} = \langle \eta_i^{\text{QMC}} \eta_j^{\text{QMC}} \rangle$, namely η_i^{QMC} is the noise already present in the i -th QMC force component. Therefore, by using that the external noise is independent from the QMC one, we obtain

$$\langle \eta_i^{\text{ext}} \eta_j^{\text{ext}} \rangle = \alpha_{ij} - \alpha_{ij}^{\text{QMC}}. \quad (64)$$

The above equation is valid at the time instant t . However, in the schemes devised in Secs. II A, II B, II C and II D, the equations of motion are discretized and integrated over a finite time step δt , and also the Langevin noise $\tilde{\eta}$ appearing in those equations is integrated over the same δt . This will slightly change the form in Eq. (64), leading to the following one:

$$\langle \tilde{\eta}_i^{\text{ext}} \tilde{\eta}_j^{\text{ext}} \rangle = \tilde{\alpha}_{ij} - \alpha_{ij}^{\text{QMC}}, \quad (65)$$

where $\tilde{\alpha}$ is the integrated noise correlator matrix, reported in Eqs. (22) and (36) for the CMPC and PIMPC-PIOUD algorithms, respectively. α^{QMC} does not need to be modified, as the expectation value of the variance-covariance QMC-force matrix in Eq. (62) is evaluated in this case during the time step δt while sampling the electron coordinates. Since the r.h.s. of Eq. (65) is a positive definite matrix (thanks to the appropriately chosen $\Delta_0 \geq \delta t$), it defines a corrected external noise which is compatible with the solution of the Langevin dynamics in both classical and quantum cases, as long as $|\mathbf{q}_{n+1} - \mathbf{q}_n|$ remains small, regardless on how large the friction is. As already mentioned, the proposed MPC schemes yield a correlated noise also affecting the conjugate variables (i. e. the nuclear positions \mathbf{q}). Therefore, the relation in Eq. (65) must be extended in the joint momentum-position coordinates. The full expression for the noise correction in the classical CPMC and quantum PIOUD integration algorithms is detailed in the Appendix A and C, respectively.

We would like to make a final comment about one of the consequences of the QMC noise contribution in our quantum algorithms. As we pointed out, the QMC-force covariance matrix α^{QMC} added in Eq. (61) makes the friction matrix γ no longer diagonal, and moreover bead dependent. In principle this violates the mathematical validity of our PIMPC integration scheme in the quantum case, because it breaks the condition $[\mathbf{K}, \gamma] = 0$. With the PIMPC propagation described in Eq. (33), we fix that issue by taking α^{QMC} as the average of the QMC covariance matrices over the beads. This constitutes a further approximation on the dynamics. On the contrary, if we simply add the whole QMC noise and its corresponding covariance into the BO friction matrix γ^{BO} , the propagator of Eq. (44) (PIOUD) is still valid, as within the

PIOUD framework every bead can have its own independent γ^{BO} in the \mathcal{L}^{BO} . This justifies again our choice to separate the physical forces subject to the QMC noise from the exact and unnoisy quantum harmonic forces, and makes PIOUD superior to PIMPC also by this technical aspect.

E. Algorithm stability with QMC forces

In the following, we shall present some calibration runs carried out with the PIOUD algorithm in the VMC framework, which will help us to set the proper simulation parameters (γ_0 , δt) and show the remarkable stability of the quantum dynamics even with noisy VMC forces for large δt and large M . The results are obtained by performing QMC-PILD short tests (about 8.5 ps of dynamics) of the Zundel ion in the gas phase at room temperature (300 K). Hereafter, the additional PIOUD parameter γ_{BO} is set to zero, to avoid overdamping in the BO propagator. The Langevin thermostat in the \mathcal{L}^{BO} part plays solely the role of correcting the BO dynamics for the intrinsic VMC noise. As we have already seen, for deterministic forces \mathcal{L}^{BO} reduces to \mathcal{L}^V , i.e. it is a simple velocity step.

For each MD step we have evaluated forces and all the energy derivatives with $\approx 3.3 \cdot 10^5$ MC samples, much larger than the total number of variational parameters ($p \approx 2.4 \cdot 10^3$) of the wave function. This allows reaching an accuracy of 1.5 mHa in the total energy per VMC energy minimization step. Between two MD steps, five QMC energy minimizations are performed with the Hessian (SRH) algorithm, in order to sample the correct BO surface. As already mentioned in Sec. III A, all variational parameters are evolved during the dynamics, except for the GTO exponents, which are kept frozen.

The optimal input friction γ_0 is chosen to minimize the potential autocorrelation time τ_V , and generate the most efficient phase space sampling during the dynamics. We shall give a general protocol to find this optimal value in the case of stochastic VMC forces, where the situation can be more complicated since the FDT is now sensitive to the QMC intrinsic noise. In our initial tests, the time step is set to 1 fs, a large value, which guarantees a quick and effective exploration of the phase space. Moreover $\gamma_{\text{BO}} = 0$ and $\Delta_0 = \delta t$, as we discovered that the most efficient simulation is the one which minimizes the damping in the BO sector. Δ_0 is taken as the minimal value which provides a positive definite γ^{BO} . In the top panel of Figure 5, we first observe that in the VMC case, the virial and the primitive kinetic energy estimators deteriorate when the applied input friction is too large ($> 0.02 \cdot 10^{-3}$ a.u.). In this situation, the additional QMC noise makes the coupling between the system and the thermostat too large to be fully controlled for such time step values ($\delta t = 1$ fs). On the other extreme, at very small γ_0 , we see that the presence of a QMC-correlated noise tends to flatten the sharp and deep

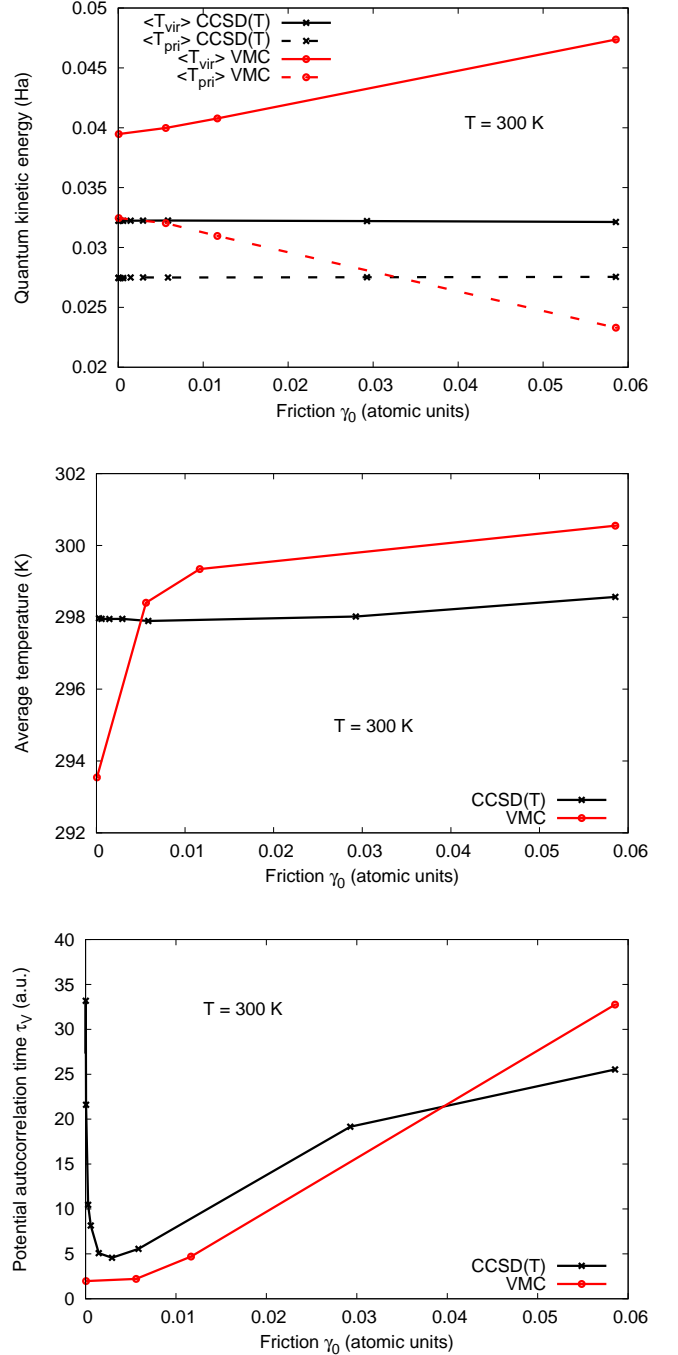


FIG. 5. PIOUD evolution of the quantum kinetic energy estimators $\langle T_{\text{vir/pri}} \rangle$ (top panel), the temperature T (middle panel) and the potential autocorrelation time τ_V (bottom panel) as a function of the input friction γ_0 . Solid lines correspond to the virial estimator of the kinetic energy whereas the primitive estimator curves are dashed. Deterministic forces are represented in black whereas the noisy QMC forces are in red. The time step and the number of quantum replicas are respectively set to $\delta t = 1$ fs and $M = 32$ beads.

minimum of the potential autocorrelation time obtained with deterministic CCSD(T) forces (bottom panel). It indicates that, contrary to the deterministic case where there is a clear advantage to set the input friction γ_0 to its optimal value, there is more freedom to choose this parameter in VMC. Indeed, the autocorrelation time divergence shown in the CCSD(T) case for small values of γ_0 disappears with VMC forces. This is due to the implicit low-value cutoff in the γ matrix provided by the intrinsic QMC noise, once the QMC-force covariance matrix is converted into an effective friction, according to Eqs.(5) and (61). In practice however, the value of γ_0 cannot be too small either, in order to avoid too cold temperatures shown in the middle panel of Fig. 5. Consequently, we need to take the largest γ_0 before the increase of the potential autocorrelation time τ_V due to the soft-modes overdamping. This will also let us recover an acceptable target temperature (see middle panel). Therefore, $\gamma_0 = 1.46 \cdot 10^{-3}$ a.u seems to be a very good compromise between autocorrelation time τ_V , effective temperature, and quality of the phase space sampling revealed by the kinetic energy estimators. All subsequent runs will be performed with that value. It is interesting to note that this is optimal for both deterministic and stochastic forces.

Similarly to the tests performed in Sec. II E with analytic CCSD(T) forces, we test here the robustness of our novel PIOUD algorithm with respect to the time step δt and to the number of quantum replicas M in the presence of noisy QMC forces. In the upper panel of Figure 6, the difference between the virial and the primitive kinetic energy estimators remains very reasonable with increasing values of the time step δt , even though the time step error is more important in the stochastic case once compared to the deterministic one. The PIOUD propagator exhibits a smaller difference between these two estimators with QMC forces than the PILE algorithm in the deterministic case. The superior performances of PIOUD will allow us to use large time steps δt .

Finally, we also check the stability of the PIOUD integration scheme with increasing number of quantum replicas M . As we can see in the bottom panel of the Figure 6, the difference between the kinetic and the primitive energy estimators is well controlled up to $M = 64$ beads in the stochastic case. On the contrary, the PILE propagator already exhibits signs of instability at this value with deterministic forces (see Figure 2). This is a further proof of the robustness of the PIOUD integrator, which is particularly recommended when one wants to perform a PILD simulation with a large number of beads with any force field, deterministic or not.

IV. RESULTS

We apply the methodology described previously in Sec. II to perform QMC-based LD and PILD simulations of the Zundel ion in the gas phase at low (50 K) and

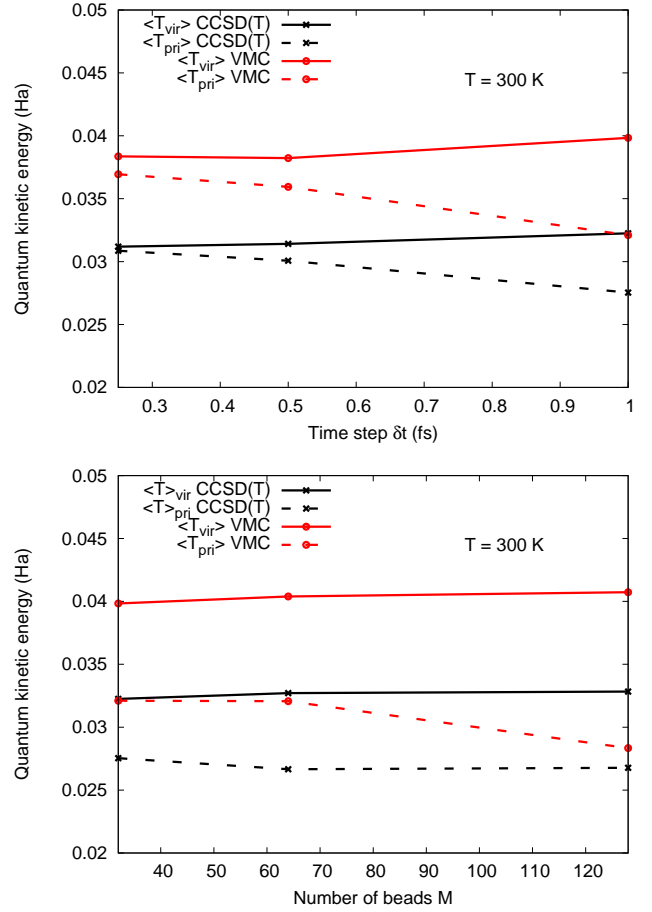


FIG. 6. PIOUD evolution of the quantum kinetic energy estimators $\langle T_{\text{vir/pri}} \rangle$ as a function of the time step δt (top panel) and the number of quantum replicas M (bottom panel). Solid lines correspond to the virial estimator of the kinetic energy whereas the primitive estimator curves are dashed. Deterministic forces are represented in black, whereas the noisy QMC forces are in red. The input friction was set to $\gamma_0 = 1.46 \cdot 10^{-3}$ a.u. fs. The default values of the time step and the number of quantum replicas are respectively $\delta t = 1$ fs and $M = 32$ beads.

room (300 K) temperature, with and without the NQE. To benchmark our results, we first carried out CMPC and PIOUD calculations using the CCSD(T) PES provided by Huang *et al*⁵³. In that case, the ionic forces are computed as finite differences of the potential energy with an increment $\delta q = 10^{-4}$ Bohr in the geometry. The dynamics is propagated with a time step $\delta t = 1$ fs until we obtain fully converged atomic distributions. As previously detailed, the input friction (γ_{BO} for CMPC, γ_0 for PIOUD) is set to $1.46 \cdot 10^{-3}$ a.u., in order to both ensure a good thermalization of the system and minimize the potential energy autocorrelation time τ_V . Consequently, that value also maximizes the diffusion of the nuclei between two subsequent LD iterations, and guarantees an efficient phase space sampling. We use 128 beads at low temperature whereas 32 beads are enough to fully recover

NQE at room temperature, which is in agreement with Ref. 81.

The QMC-LD (CMPC) and QMC-PILD (PIOUD) simulations are performed using the wave function of Ref. 86 as a starting point for the dynamics. Unless otherwise specified, all calculations are carried out by bead-grouping the VMC parameters with $N_{\text{groups}} = 1$, namely with the same wave function parameters shared by all the replicas at a given iteration. The QMC statistics is the same as the one used in the stability tests (Sec. III E). The equations of motion are propagated with a large time step $\delta t = 1$ fs to explore the phase space as fast as possible without doing too many evaluations of the wave function. We stopped the production run after 20 ps of dynamics, which is the minimum required to obtain converged results⁹⁸. At the end of each simulation, the average temperature, the virial and primitive kinetic energy estimators, the energy fluctuations, and the evolution of the energy gradients with respect to the electronic parameters are checked to ensure the reliability of the simulation. In order to follow the correct BO energy landscape, we require that the error made on the temperature and the kinetic energy must not exceed 5%, whereas the values of the energy gradients with respect to the wave function parameters must be lower than 3-4 times their standard deviation.

In Figures 7 and 8 we present the normalized oxygen-oxygen (g_{OO}) and oxygen-proton (g_{OH}) distributions as a function of the inter-oxygen distance. These distributions are obtained at low and room temperature with and without quantum nuclei. Both the VMC and benchmark CCSD(T) results are shown.

We first observe a very good overall agreement between the radial correlation functions g_{OO} and g_{OH} obtained with the reference CCSD(T) calculations and our VMC-based simulations. We notice that at 50 K, quantum effects renormalize the height of the g_{OO} peak by a factor of 3, while the g_{OH} distribution is renormalized by a factor of 2 with respect to its classical counterpart. The NQE have thus a huge effect in the oxygen-oxygen distribution function because the classical system is almost frozen around its zero temperature equilibrium configuration, whereas the ZPE leads to strong quantum fluctuations even at low temperature.

At 300 K, even though NQE are much less significant for the oxygen-oxygen distribution, they are still very important for the oxygen-proton correlation function, where the shapes of the distributions obtained in the classical and in the quantum case are very different. Indeed, the classical g_{OH} distribution is asymmetric around the equilibrium distance, whereas the quantum correlation function is symmetric with much longer tails, indicating the possibility of instantaneous proton hoppings by quantum tunneling. On the contrary, NQE are less dramatic at room temperature for the g_{OO} radial distribution, as expected from the greater mass of the oxygen atoms which diminishes the thermal de Broglie wavelength.

In the classical case, the intrinsic noise present in the

QMC forces tends to spoil the sampling of the instantaneous oxygen-oxygen and oxygen-proton distances, which has to be very accurate because the resulting distributions are extremely sharp. In the quantum case, instead, the QMC noise is helpful in improving the quantum delocalization of the nuclei in the desired regions of the phase space. The phase space sampling efficiency seems to be enhanced in the quantum case with respect to the classical one. The quantum results are unexpectedly easier to converge, and they yield radial distributions with reduced error bars compared to their classical counterparts.

Our benchmark system is ideal also to check out the quality of the bead-grouping technique described in Sec. III B for the electronic parameters in *ab initio* VMC-PIOUD simulations. At room temperature the bead-grouping with $N_{\text{groups}} = 1$ works very well, giving results on the top of the CCSD(T) reference. At low temperature, the agreement between the CCSD(T) reference and the VMC-PIOUD results with $N_{\text{groups}} = 1$ is still good, although some minor discrepancies appear in the tails of the oxygen-oxygen and oxygen-proton distributions. The strongest bias, though still quantitatively acceptable, is present in the g_{OH} function, as this pair distribution is the most sensitive to quantum delocalization effects. By increasing N_{groups} to 16, we improve the peak positions of both g_{OH} and g_{OO} , and the error made in the their tails becomes almost negligible.

This can be simply interpreted by considering the quantum-to-classical isomorphism: hydrogen atoms have a light mass, so the corresponding ring polymers are much more spread than the ones mimicking the quantum nuclei of oxygen. Consequently, the bead-grouping approximation on the optimal electronic parameters $\{\lambda_{\text{av}}^{(l)}\}_{l=1,\dots,N_{\text{groups}}}$ is more severe for hydrogen than for oxygen. The resulting potential energy landscape is thus affected, and displays a larger curvature around its minimum, due to the energy penalty given by the non fully-optimized wave functions, being the worst for those beads which are the farthest from the centroid. This effect is apparent in the slightly shorter tails of the radial correlation function, since the corresponding ionic configurations are less visited as they have higher energies. Therefore, a compromise must be found by minimizing the total amount of CPU time spent for a simulation and the desired target accuracy on the structural and static properties of the system. While at 50 K an $N_{\text{groups}} > 1$ should be chosen, at 300 K $N_{\text{groups}} = 1$ gives very accurate results. Thus, at room temperature we are able to carry out a reliable and very accurate fully-quantum dynamics of the Zundel cation in almost the same CPU time as for classical nuclei.

Finally, it is also interesting to quantify NQE versus thermal effects, by observing the evolution of the radial correlation functions at increasing temperature or when the quantum delocalization of the nuclei is taken into account. For classical particles, there is a clear broadening of the g_{OO} and g_{OH} distribution with increasing temperature. Indeed, there are more molecular vibra-

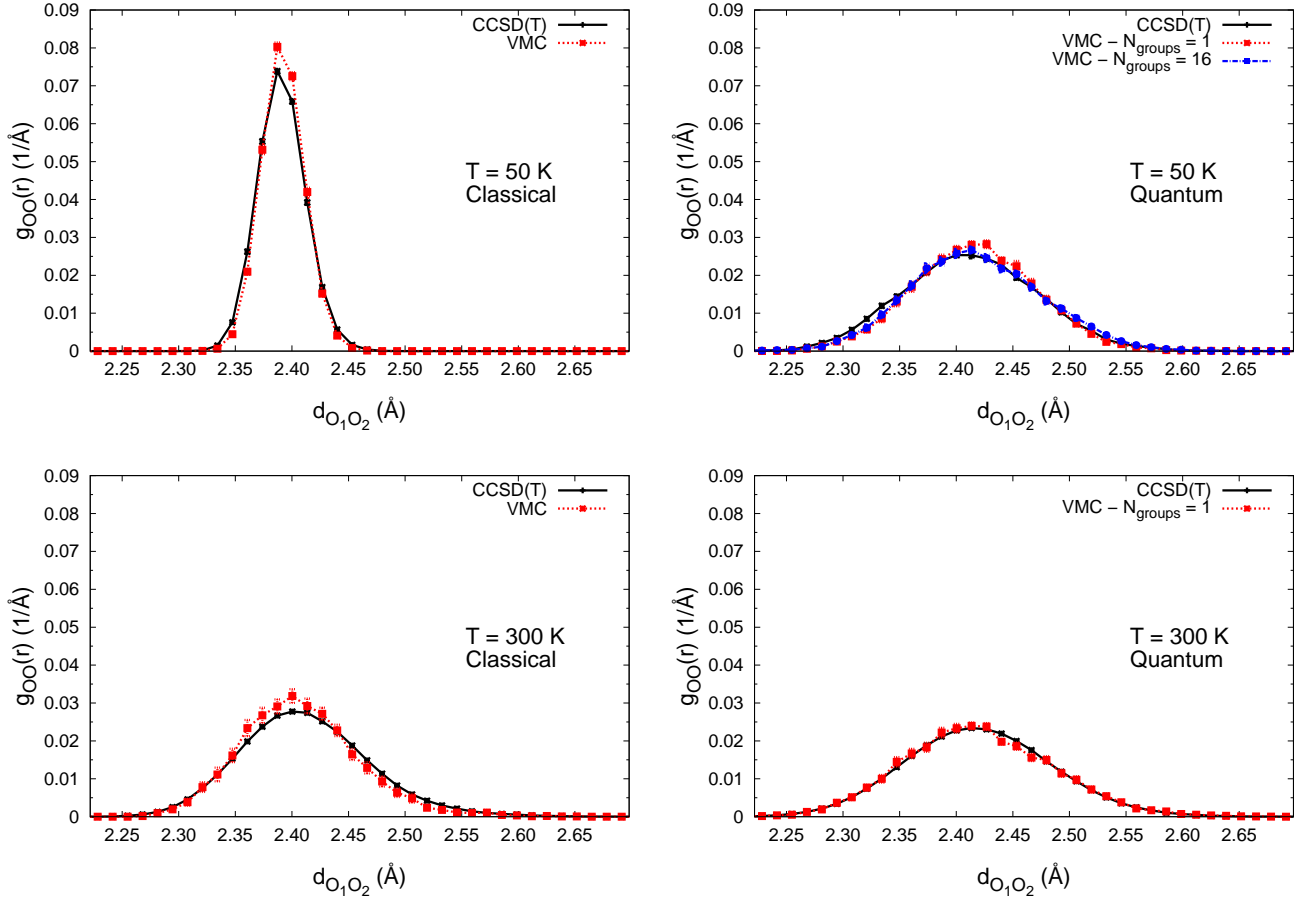


FIG. 7. Normalized oxygen-oxygen distributions obtained by CMPC-LD (left) and PIOUD (right) simulations at low temperature $T = 50$ K (top) and $T = 300$ K (bottom). The black curves represent the distributions obtained with analytic CCSD(T) forces which are almost exact, whereas the red and blue curves correspond to VMC-(PI)LD dynamics with $N_{\text{groups}} = 1$ and $N_{\text{groups}} = 16$ respectively. Quantum simulations are performed with $M = 128$ beads at $T = 50$ K and $M = 32$ beads at $T = 300$ K. The friction is set to $\gamma_0 = 1.46 \cdot 10^{-3}$ a.u.

tions because the entropy is increased and the instantaneous oxygen-oxygen and oxygen-proton distances are subject to enhanced fluctuations. This is confirmed by examining Figure 9, where we plot the oxygen-proton distance for the two oxygen sites as a function of the inter-oxygen distance. Dagrada and coworkers⁸⁶ have shown that QMC techniques are in excellent agreement with the reference CCSD(T) geometries at zero temperature. The minimum energy configuration of the Zundel cation is symmetric (C_2 symmetry) with the proton at the middle at the oxygen-oxygen distance. At $T = 50$ K, the classical proton remains extremely localized around the C_2 -symmetry geometric minimum which leads to a very sharp distribution, reported in the upper left panels of Figures 7 and 8. At $T = 300$ K, the system has more thermal energy to visit asymmetric configurations with longer oxygen-oxygen distance and the excess proton sitting closer to one oxygen than to the other. This is represented by the two branches in the lower left panel of Figure 9. Even in this situation the symmetric config-

urations are more often explored than the phase regions forming the two wings.

On the contrary, thermal effects are much less important when NQE are taken into account, as apparent from the right panels of Figures 7, 8 and 9, which show very similar correlation functions for both temperatures. Indeed, quantum fluctuations make the proton able to easily jump to a neighbor oxygen site by quantum tunneling, recovering a more symmetric behavior. This is characterized by longer tails in the g_{OH} distribution function compared with the classical ones at $T = 300$ K, and by the absence of wings in Fig. 9. Moreover, the 2D distributions are nearly the same at low and room temperature. These conclusions are in agreement with previous studies on this system^{81,82}. Some calculations performed with deterministic forces obtained from the reference CCSD(T) PES show that thermal effects start to be significant for temperatures greater than $T = 900$ K. This confirms that NQE are essential to fully understand the microscopic mechanisms involving the proton

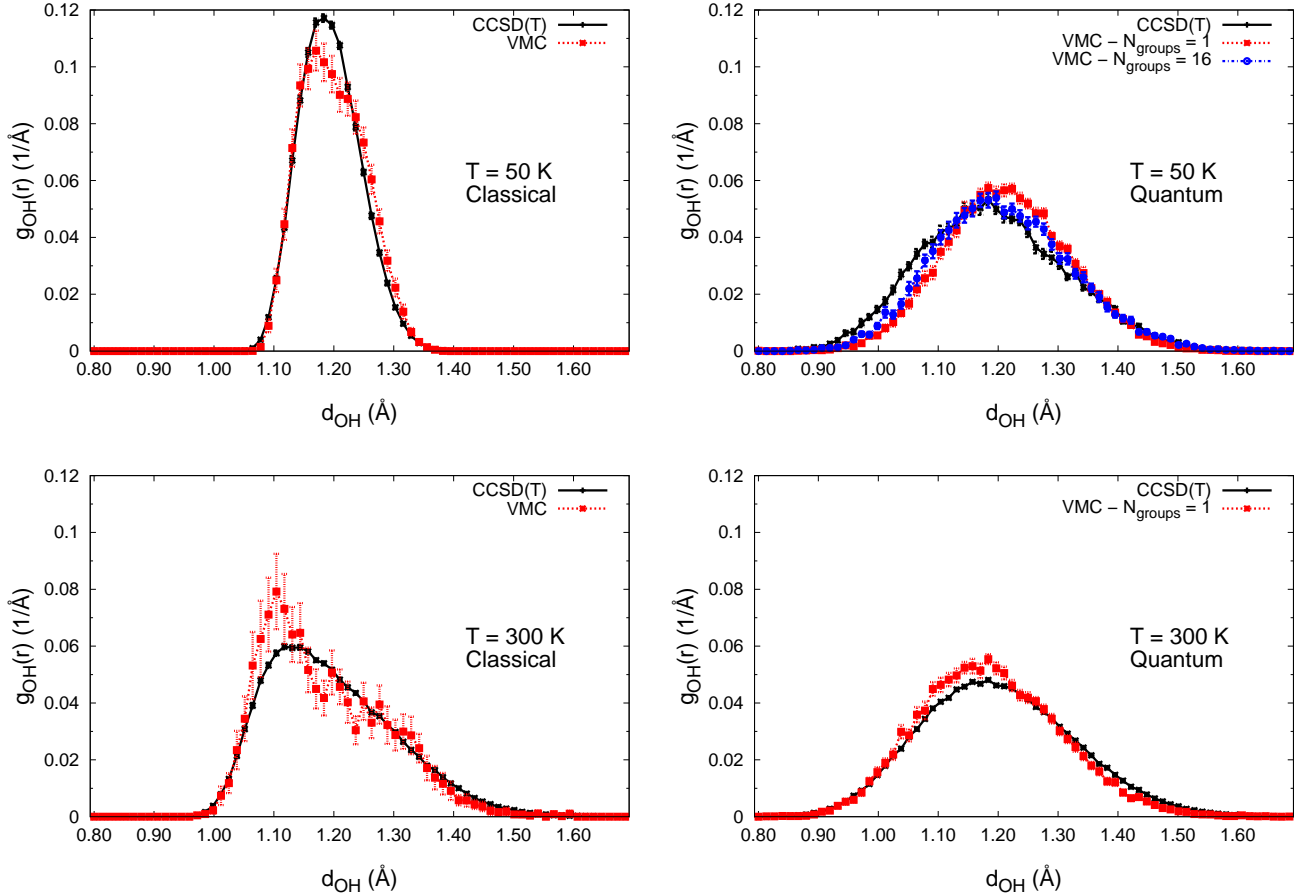


FIG. 8. Normalized oxygen-proton distributions obtained by CMPC-LD (left) and PIOUD (right) simulations at low temperature $T = 50$ K (top) and $T = 300$ K (bottom). The black curves represent the distributions obtained with analytic CCSD(T) forces which are almost exact, whereas the red and blue curves correspond to VMC-(PI)LD dynamics with $N_{\text{groups}} = 1$ and $N_{\text{groups}} = 16$ respectively. Quantum simulations are performed with $M = 128$ beads at $T = 50$ K and $M = 32$ beads at $T = 300$ K. The friction is set to $\gamma_0 = 1.46 \cdot 10^{-3}$ a.u.

dynamics in liquid water at ambient conditions.

V. CONCLUSIONS

In this paper, we have extended the previous QMC-driven classical LD formalism (CMPC) to quantum nuclei. We have demonstrated the possibility to deal with the intrinsic QMC noise in the ionic forces evaluation by incorporating this possible source of bias into a PILD formalism. By fulfilling the FDT in a generalized framework, we correct the quantum dynamics for the QMC noise. We are thus able to perform simulations of QMC correlated electrons coupled with quantum nuclei.

From the theoretical side, we work with joint momentum-position coordinates and exploit a Trotter breakup between the physical vibrations, set by the BO surface, and the harmonic ones, introduced by the quantum-to-classical isomorphism. This allows us to separate the dynamics driven by the BO forces, from the

harmonic one of the free ring polymers coupled with the Langevin thermostat. In our approach, the latter dynamics is propagated exactly, as the resulting stochastic differential equations are linear in both momenta and positions. This step corresponds to an Ornstein-Uhlenbeck process, while in the case of QMC forces, the noise correction is performed in the former BO step. The resulting algorithm is the Path Integral Ornstein Uhlenbeck Dynamics (PIOUD).

As a first application, we took the Zundel ion, a benchmark system, and compared its quantum nuclear dynamics driven by VMC forces with the one evolved according to a deterministic PES, obtained at the accurate CCSD(T) level of theory. In the case of deterministic CCSD(T) forces, we have shown that our novel PIOUD algorithm has properties similar to the PILE scheme as far as the potential autocorrelation time τ_V and the algorithmic diffusion constant D are concerned. Moreover, PIOUD features a larger stability range as a function of both time step δt and number of quantum replicas M .

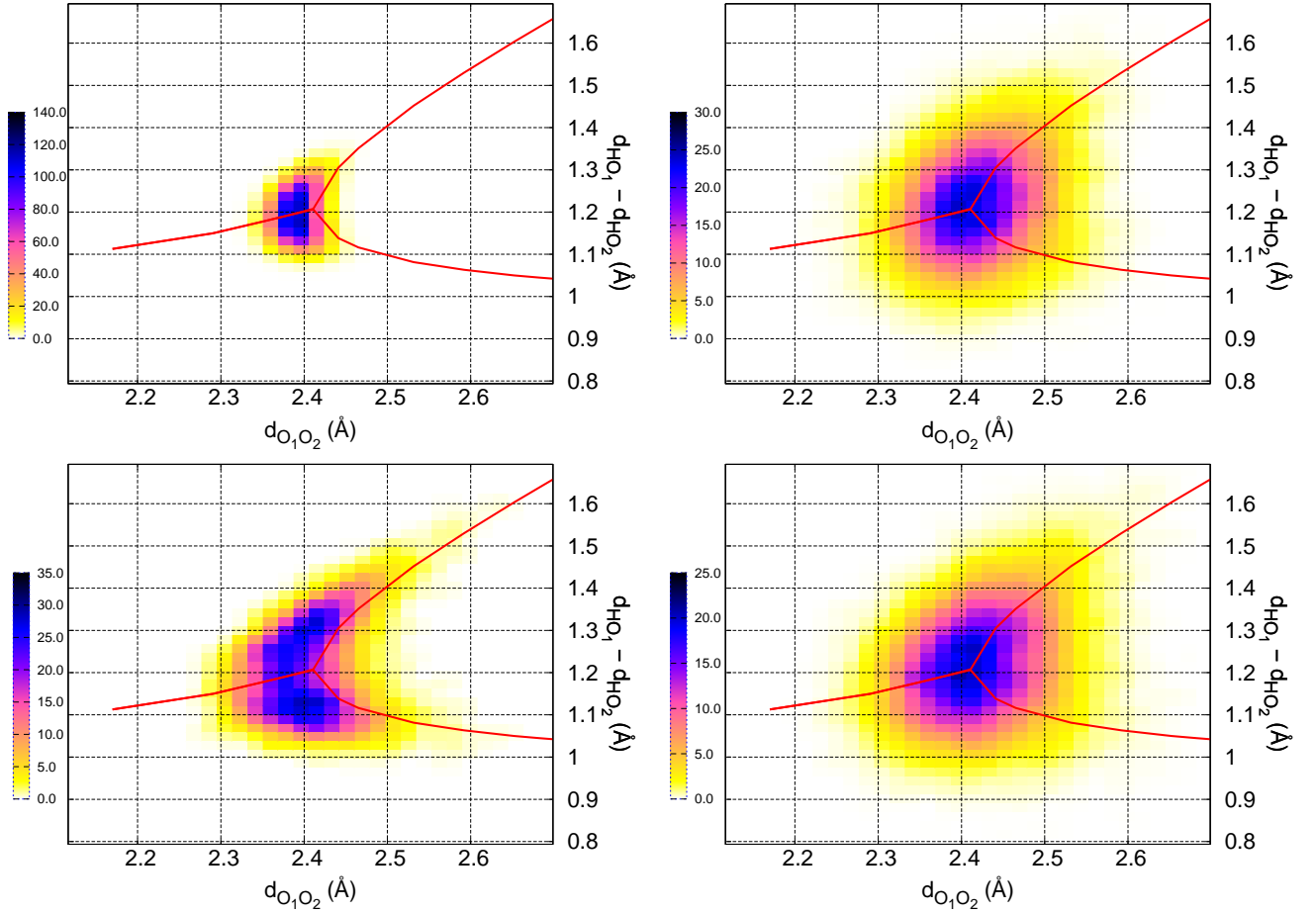


FIG. 9. Bidimensional oxygen-oxygen and oxygen-proton distributions obtained by QMC-driven CMPC-LD (left) and PIOUD (right) simulations at low temperature $T = 50$ K (top) and $T = 300$ K (bottom). The red curve corresponds to the equilibrium geometries of the Zundel ion at zero temperature obtained by CCSD(T) calculations (from Ref. 86). Quantum simulations are performed with $M = 128$ beads at $T = 50$ K and $M = 32$ beads at $T = 300$ K. The friction is set to $\gamma_0 = 1.46 \cdot 10^{-3}$ a.u.

This is encouraging, since with its improved stability, PIOUD can visit the phase space in a more efficient way, no matter whether the forces are deterministic or not.

We further verified the stability of our approach in the stochastic case, where the PES is computed by VMC during a short nuclear dynamics. Then, we carried out extensive VMC simulations at low (50 K) and room (300 K) temperatures of the Zundel complex with both classical and quantum nuclei, by means of the CMPC and PIOUD algorithms, respectively. The outcome of the calculations in this model system suggests that even at room temperature the NQE are crucial to reach a quantitative description of proton transfer in water and aqueous systems. Indeed, NQE take over thermal effects not only at 50 K but also at 300 K, and contribute to a greater proton mobility by quantum tunneling. A very good agreement with the CCSD(T) reference calculations is found, even in the coarsest (and most effective) bead-grouping approximation, where the same electron VMC parameters are shared by all quantum replicas.

This work proves the potential of QMC methods com-

bined with the PILD approach to perform fully quantum calculations of water-like and aqueous systems. In the perspective of performing such simulations on larger systems, our novel scheme overcomes two major scalability problems. On the one hand, it benefits from the QMC reasonable scaling with respect to the number of electrons contrary to other advanced electronic structure methods. On the other hand, using the bead-grouping technique, we are able to carry out fully *ab initio* dynamics of the Zundel ion with almost the same computational cost as for classical nuclei, without deteriorating NQE. Within this approximation, the quantum simulations are paradoxically more efficient than their classical counterparts. Indeed, the nuclear observables statistics is improved, because the phase space is more efficiently explored, thanks to the quantum fluctuations included in the framework, while the QMC statistical fluctuations of the electronic part are not detrimental, as they are averaged over the beads. Consequently, this work paves the way to study, at the theoretical level, proton transfer mechanisms in more complex water clusters, starting, for instance, with

the protonated water hexamer $\text{H}_{13}\text{O}_6^+$, and the larger $\text{H}_{43}\text{O}_{21}^+$ cluster, where the excess proton localization is still under debate. Similar ideas developed in this work for the application of the molecular dynamics to describe NQE, can be used within the recently proposed "accelerated molecular dynamics" based on first order Langevin equation.⁹⁹

ACKNOWLEDGEMENTS

We thank Joel M. Bowman and Xinchuan Huang for providing us with the coupled cluster potential energy surface of H_5O_2^+ . F.M. thanks Mario Dagrada for sharing with us the optimal H_5O_2^+ wave function at zero temperature, and for helpful discussions. We also acknowledge computational resources provided by the PRACE preparatory access number 2010PA2475 and PRACE project number 2015133179. This work was granted access to the HPC resources of TGCC and IDRIS under the allocation 2016-096493 made by GENCI.

Appendix A: Noise correction in the classical case

We detail in this section the noise correction which needs to be applied if one wants to include QMC noise into the Langevin dynamics without inducing a bias on the final target temperature. Analogously to the equation (63), the integrated noise can be written

$$\begin{aligned}\tilde{\eta}_i &= \tilde{\eta}_i^{\text{ext}} + \tilde{\eta}_i^{\text{QMC}}, \\ \tilde{\tilde{\eta}}_i &= \tilde{\tilde{\eta}}_i^{\text{ext}} + \tilde{\tilde{\eta}}_i^{\text{QMC}}.\end{aligned}\quad (\text{A1})$$

Therefore, still assuming that the external noise is independent from the QMC noise, we obtain very similar relations to Eq.(64):

$$\begin{aligned}\langle (\tilde{\eta}^{\text{ext}})^T \tilde{\eta}^{\text{ext}} \rangle &= \tilde{\alpha}_{11} - \alpha^{\text{QMC}}, \\ \langle (\tilde{\tilde{\eta}}^{\text{ext}})^T \tilde{\tilde{\eta}}^{\text{ext}} \rangle &= \tilde{\alpha}_{22} - \alpha^{\text{QMC}}, \\ \langle (\tilde{\eta}^{\text{ext}})^T \tilde{\tilde{\eta}}^{\text{ext}} \rangle &= \tilde{\alpha}_{12} - \alpha^{\text{QMC}},\end{aligned}\quad (\text{A2})$$

where the explicit expressions of the $\tilde{\alpha}$ matrix components have been given in the main text in Eq. (22). By simply computing the square root of this 2×2 matrix which is positive definite by construction, we are able to evaluate explicitly the exact integrated external noise to propagate the dynamics.

Appendix B: Quantum integration scheme

We detail in this section the mathematical derivation of our novel integrator described in section II C and the explicit formulas of the $\mathbf{\Lambda}$, $\mathbf{\Gamma}$ and $\mathbf{\Theta}$ matrices. For the following algebra, it is useful to evaluate the inverse of the matrix $\hat{\gamma}$

$$\hat{\gamma}^{-1} = \begin{pmatrix} \mathbf{0} & -\mathbf{I} \\ \mathbf{K}^{-1} & \mathbf{K}^{-1}\gamma \end{pmatrix}. \quad (\text{B1})$$

In order to solve the differential system in Eq. (15) for a generic time step δt in the quantum case, we need to exponentiate the matrix $\hat{\gamma}$. Using the fundamental assumption $[\mathbf{K}, \gamma] = 0$ previously justified in the paper, we consider each common eigenvector of \mathbf{K} and γ that can correspond to a joint momentum and coordinate mode. In this two-fold basis, the matrix $\hat{\gamma}$ is a simple 2×2 block matrix where as K and γ are just numbers. The block matrix $\hat{\gamma}$ can be more conveniently rewritten in terms of the Pauli matrices $\sigma_x, \sigma_y, \sigma_z$:

$$\begin{aligned}\hat{\gamma} &= \frac{\gamma}{2}\mathbf{I} + \mathbf{x} \\ \mathbf{x} &= \begin{pmatrix} \frac{\gamma}{2} & K \\ -1 & -\frac{\gamma}{2} \end{pmatrix} \\ &= \frac{K-1}{2}\sigma_x + i\frac{K+1}{2}\sigma_y + \frac{\gamma}{2}\sigma_z.\end{aligned}\quad (\text{B2})$$

Then, the exponentiation can be straightforwardly obtained, by using standard Pauli matrices algebra

$$e^{\hat{\gamma}\delta t} = e^{\frac{\gamma\delta t}{2}} \begin{cases} \cosh(|x|\delta t)\mathbf{I} + \frac{\mathbf{x}}{|x|}\sinh(|x|\delta t) & \text{for } \gamma^2 \geq 4K \\ \cos(|x|\delta t)\mathbf{I} + \frac{\mathbf{x}}{|x|}\sin(|x|\delta t) & \text{for } \gamma^2 < 4K \end{cases} \quad (\text{B3})$$

where $|x| = \sqrt{|\gamma^2/4 - K|}$. Recombining Eq.(B1) and Eq.(B3) one obtains:

$$\hat{\gamma}^{-1}(\mathbf{I} - e^{-\hat{\gamma}\delta t}) = \begin{pmatrix} e^{-\frac{\gamma\delta t}{2}} \frac{\sinh(|x|\delta t)}{|x|} & -(1 - e^{-\frac{\gamma\delta t}{2}} \cosh(|x|\delta t)) + \gamma e^{-\frac{\gamma\delta t}{2}} \frac{\sinh(|x|\delta t)}{2|x|} \\ 1 - e^{-\frac{\gamma\delta t}{2}} \frac{\cosh(|x|\delta t)}{K} - \gamma e^{-\frac{\gamma\delta t}{2}} \frac{\sinh(|x|\delta t)}{2K|x|} & \gamma(1 - e^{-\frac{\gamma\delta t}{2}} \frac{\cosh(|x|\delta t)}{K}) + (1 - \frac{\gamma^2}{2K})e^{-\frac{\gamma\delta t}{2}} \frac{\sinh(|x|\delta t)}{|x|} \end{pmatrix} \quad (\text{B4})$$

for $\gamma^2 > 4K$, while for $\gamma^2 \leq 4K$:

$$\hat{\gamma}^{-1}(\mathbf{I} - e^{-\hat{\gamma}\delta t}) = \begin{pmatrix} e^{-\frac{\gamma\delta t}{2}} \frac{\sin(|x|\delta t)}{|x|} & -(1 - e^{-\frac{\gamma\delta t}{2}} \cos(|x|\delta t)) + \frac{\gamma e^{-\frac{\gamma\delta t}{2}} \sin(|x|\delta t)}{2|x|} \\ \frac{1 - e^{-\frac{\gamma\delta t}{2}} \cos(|x|\delta t)}{K} - \frac{\gamma e^{-\frac{\gamma\delta t}{2}} \sin(|x|\delta t)}{2K|x|} & \frac{\gamma(1 - e^{-\frac{\gamma\delta t}{2}} \cos(|x|\delta t))}{K} + (1 - \frac{\gamma^2}{2K}) \frac{e^{-\frac{\gamma\delta t}{2}} \sin(|x|\delta t)}{|x|} \end{pmatrix}. \quad (\text{B5})$$

Finally, for the case $\gamma^2 > 4K$, we obtain:

$$\begin{aligned}\Gamma &= e^{-\frac{\gamma}{2}\delta t} \frac{\sinh(|x|\delta t)}{|x|} \\ \Theta &= \frac{1 - e^{-\frac{\gamma\delta t}{2}} \cosh(|x|\delta t)}{K} - \frac{\gamma e^{-\frac{\gamma\delta t}{2}} \sinh(|x|\delta t)}{2K|x|} \\ \Lambda &= e^{-\frac{\gamma\delta t}{2}} \begin{pmatrix} \cosh(|x|\delta t) - \frac{\gamma}{2} \frac{\sinh(|x|\delta t)}{|x|} & -K \frac{\sinh(|x|\delta t)}{|x|} \\ \frac{\sinh(|x|\delta t)}{|x|} & \cosh(|x|\delta t) + \frac{\gamma \sinh(|x|\delta t)}{2|x|} \end{pmatrix},\end{aligned}\tag{B6}$$

while for $\gamma^2 \leq 4K$, we have:

$$\begin{aligned}\Gamma &= e^{-\frac{\gamma}{2}\delta t} \frac{\sin(|x|\delta t)}{|x|} \\ \Theta &= \frac{1 - e^{-\frac{\gamma\delta t}{2}} \cos(|x|\delta t)}{K} - \frac{\gamma e^{-\frac{\gamma\delta t}{2}} \sin(|x|\delta t)}{2K|x|} \\ \Lambda &= e^{-\frac{\gamma\delta t}{2}} \begin{pmatrix} \cos(|x|\delta t) - \frac{\gamma}{2} \frac{\sin(|x|\delta t)}{|x|} & -K \frac{\sin(|x|\delta t)}{|x|} \\ \frac{\sin(|x|\delta t)}{|x|} & \cos(|x|\delta t) + \frac{\gamma \sin(|x|\delta t)}{2|x|} \end{pmatrix}.\end{aligned}\tag{B7}$$

To evaluate the time-integrated noise covariance matrix $\tilde{\alpha}$ in the quantum case, defined by Eq. (36), namely $\tilde{\alpha} \equiv \langle \mathbf{E}_{\text{int}}^T \mathbf{E}_{\text{int}} \rangle$, it is useful to introduce the following integral:

$$\Gamma_z = \int_{-\delta t}^0 dt e^{zt} = \frac{1 - e^{-z\delta t}}{z}.\tag{B8}$$

By using Eq. (B3), it is straightforward to carry out the integrals to obtain

$$\begin{aligned}\tilde{\alpha} &= \frac{\Gamma_{\gamma+2|x|} + \Gamma_{\gamma-2|x|} + 2\Gamma_\gamma}{4} \hat{\alpha} \\ &+ \frac{\mathbf{x}\hat{\alpha}\mathbf{x}^\dagger}{|x|^2} \frac{\Gamma_{\gamma+2|x|} + \Gamma_{\gamma-2|x|} - 2\Gamma_\gamma}{4} \\ &+ \frac{\hat{\alpha}\mathbf{x}^\dagger + \mathbf{x}\hat{\alpha}}{|x|} \frac{\Gamma_{\gamma+2|x|} - \Gamma_{\gamma-2|x|}}{4}\end{aligned}\tag{B9}$$

for $\gamma^2 \geq 4K$, whereas for $\gamma^2 \leq 4K$ we obtain a very similar formula where $|x|$ is replaced by $i|x|$:

$$\begin{aligned}\tilde{\alpha} &= \frac{\Gamma_{\gamma+2i|x|} + \Gamma_{\gamma-2i|x|} + 2\Gamma_\gamma}{4} \hat{\alpha} \\ &- \frac{\mathbf{x}\hat{\alpha}\mathbf{x}^\dagger}{|x|^2} \frac{\Gamma_{\gamma+2i|x|} + \Gamma_{\gamma-2i|x|} - 2\Gamma_\gamma}{4} \\ &- i \frac{\hat{\alpha}\mathbf{x}^\dagger + \mathbf{x}\hat{\alpha}}{|x|} \frac{\Gamma_{\gamma+2i|x|} - \Gamma_{\gamma-2i|x|}}{4}.\end{aligned}\tag{B10}$$

$\hat{\alpha}$ has been defined in Eq. (37). In order to conclude the analytic derivation of the quantum integration scheme, we also give the explicit expression of the two further matrices appearing in the Eq. (B9) and Eq. (B10):

$$\begin{aligned}\mathbf{x}\hat{\alpha}\mathbf{x}^\dagger &= \begin{pmatrix} \frac{\gamma^2\alpha}{4} & -\frac{\gamma\alpha}{2} \\ -\frac{\gamma\alpha}{2} & \alpha \end{pmatrix}, \\ \hat{\alpha}\mathbf{x}^\dagger + \mathbf{x}\hat{\alpha} &= \begin{pmatrix} \gamma & -\alpha \\ -\alpha & 0 \end{pmatrix}.\end{aligned}\tag{B11}$$

Appendix C: Noise correction in the quantum case

Similarly to the classical case, the QMC noise has to be disentangled from the total noise according to Eq. (63). Since we have derived an analytic expression of the noise matrix at the end of the previous paragraph, we are now able to evaluate the external noise correlation matrix which is nothing but the generalization of Eq.(64) to the quantum case:

$$\alpha^{\text{ext}} = \langle (\eta^{\text{ext}})^T \eta^{\text{ext}} \rangle = \begin{pmatrix} \frac{\tilde{\alpha}_{11}}{\Gamma^2} - \alpha^{\text{QMC}} & \frac{\tilde{\alpha}_{12}}{\Gamma\Theta} - \alpha^{\text{QMC}} \\ \frac{\tilde{\alpha}_{12}}{\Gamma\Theta} - \alpha^{\text{QMC}} & \frac{\tilde{\alpha}_{22}}{\Theta^2} - \alpha^{\text{QMC}} \end{pmatrix}.\tag{C1}$$

* felix.mouhat@impmc.upmc.fr

¹ M. Eigen, *Angew. Chem. Int. Ed.* **3**, 1 (1964).

² O. F. Mohammed, D. Pines, J. Dreyer, E. Pines, and E. T. J. Nibbering, *Science* **310**, 83 (2005).

- ³ O. F. Mohammed, D. Pines, E. Pines, and E. T. Nibbering, *Chem. Phys.* **341**, 240 (2007).
- ⁴ A. Hassanali, M. K. Prakash, H. Eshet, and M. Parrinello, *Proceedings of the National Academy of Sciences* **108**, 20410 (2011).
- ⁵ S. H. Lee and J. C. Rasaiah, *J. Chem. Phys.* **135**, 124505 (2011).
- ⁶ N. Agmon, H. J. Bakker, R. K. Campen, R. H. Henchman, P. Pohl, S. Roke, M. Thämer, and A. Hassanali, *Chem. Rev.* **116**, 7642 (2016).
- ⁷ D. Riccardi, P. König, X. Prat-Resina, H. Yu, M. Elstner, T. Frauenheim, and Q. Cui, *J. Am. Chem. Soc.* **128**, 16302 (2006).
- ⁸ D. Riccardi, S. Yang, and Q. Cui, *Biochimica et Biophysica Acta (BBA) - Proteins and Proteomics* **1804**, 342 (2010).
- ⁹ C. A. Wright, *Biochimica et Biophysica Acta (BBA) - Bioenergetics* **1757**, 886 (2006).
- ¹⁰ T. E. Decoursey, *Physiol. Rev.* **83**, 475 (2003).
- ¹¹ E. Freier, S. Wolf, and K. Gerwert, *Proc. Natl. Acad. Sci. U.S.A.* **108**, 11435 (2011).
- ¹² B. J. Gertner and J. T. Hynes, *Faraday Disc.* **110**, 301 (1998).
- ¹³ D. Marx, *ChemPhysChem* **7**, 1848 (2006).
- ¹⁴ A. A. Hassanali, J. Cuny, V. Verdolino, and M. Parrinello, *Philosophical Transactions of the Royal Society A: Mathematical, Physical and Engineering Sciences* **372**, 20120482 (2014).
- ¹⁵ W. L. Jorgensen, J. Chandrasekhar, J. D. Madura, R. W. Impey, and M. L. Klein, *J. Chem. Phys.* **79**, 926 (1983).
- ¹⁶ M. Sprik, *J. Phys. Chem.* **95**, 2283 (1991).
- ¹⁷ M. W. Mahoney and W. L. Jorgensen, *J. Chem. Phys.* **112**, 8910 (2000).
- ¹⁸ P. L. Silvestrelli and M. Parrinello, *J. Chem. Phys.* **111**, 3572 (1999).
- ¹⁹ J. C. Grossman, E. Schwegler, E. W. Draeger, F. Gygi, and G. Galli, *J. Chem. Phys.* **120**, 300 (2004).
- ²⁰ J. VandeVondele, F. Mohamed, M. Krack, J. Hutter, M. Sprik, and M. Parrinello, *J. Chem. Phys.* **122**, 014515 (2005).
- ²¹ R. Jonchiere, A. P. Seitsonen, G. Ferlat, A. M. Saitta, and R. Vuilleumier, *J. Chem. Phys.* **135**, 154503 (2011).
- ²² P. Carloni, U. Rothlisberger, and M. Parrinello, *Acc. Chem. Res.* **35**, 455 (2002).
- ²³ R. A. Friesner and B. D. Dunietz, *Acc. Chem. Res.* **34**, 351 (2001).
- ²⁴ S. Yoo, X. C. Zeng, and S. S. Xantheas, *J. Chem. Phys.* **130**, 221102 (2009).
- ²⁵ H.-S. Lee and M. E. Tuckerman, *J. Chem. Phys.* **126**, 164501 (2007).
- ²⁶ I.-C. Lin, A. P. Seitsonen, I. Tavernelli, and U. Rothlisberger, *J. Chem. Theory Comput.* **8**, 3902 (2012).
- ²⁷ B. Santra, R. A. DiStasio, F. Martelli, and R. Car, *Molecular Physics* **113**, 2829 (2015).
- ²⁸ M. J. Gillan, D. Alfè, and A. Michaelides, *J. Chem. Phys.* **144**, 130901 (2016).
- ²⁹ S. Y. Willow, M. A. Salim, K. S. Kim, and S. Hirata, *Sci. Rep.* **5**, 14358 (2015).
- ³⁰ M. J. Gillan, F. R. Manby, M. D. Towler, and D. Alfè, *J. Chem. Phys.* **136**, 244105 (2012).
- ³¹ N. A. Benedek, I. K. Snook, M. D. Towler, and R. J. Needs, *The Journal of Chemical Physics* **125**, 104302 (2006).
- ³² C. Pierleoni, D. M. Ceperley, and M. Holzmann, *Phys. Rev. Lett.* **93** (2004).
- ³³ C. Pierleoni and D. Ceperley, "The coupled electron-ion monte carlo method," in *Computer Simulations in Condensed Matter Systems: From Materials* edited by M. Ferrario, G. Ciccotti, and K. Binder (Springer Berlin Heidelberg, Berlin, Heidelberg, 2006) pp. 641–683.
- ³⁴ C. Attaccalite and S. Sorella, *Phys. Rev. Lett.* **100** (2008).
- ³⁵ G. Mazzola, S. Yunoki, and S. Sorella, *Nat Comms* **5** (2014).
- ³⁶ A. Zen, Y. Luo, G. Mazzola, L. Guidoni, and S. Sorella, *J. Chem. Phys.* **142**, 144111 (2015).
- ³⁷ J. A. Morrone and R. Car, *Phys. Rev. Lett.* **101** (2008).
- ³⁸ C. Vega, M. M. Conde, C. McBride, J. L. F. Abascal, E. G. Noya, R. Ramirez, and L. M. Sesé, *J. Chem. Phys.* **132**, 046101 (2010).
- ³⁹ B. Pamuk, J. M. Soler, R. Ramírez, C. P. Herrero, P. W. Stephens, P. B. Allen, and M.-V. Fernández-Serra, *Phys. Rev. Lett.* **108** (2012).
- ⁴⁰ L. Kong, X. Wu, and R. Car, *Phys. Rev. B* **86** (2012).
- ⁴¹ F. Giberti, A. A. Hassanali, M. Ceriotti, and M. Parrinello, *J. Phys. Chem. B* **118**, 13226 (2014).
- ⁴² G. Zundel and H. Metzger, *Z. Phys. Chem.* **58**, 225 (1968).
- ⁴³ D. Wei and D. R. Salahub, *J. Chem. Phys.* **101**, 7633 (1994).
- ⁴⁴ M. E. Tuckerman, D. Marx, M. L. Klein, and M. Parrinello, *Science* **275**, 817 (1997).
- ⁴⁵ R. Vuilleumier and D. Borgis, *J. Phys. Chem. B* **102**, 4261 (1998).
- ⁴⁶ R. Vuilleumier and D. Borgis, *Journal of molecular structure* **552**, 117 (2000).
- ⁴⁷ E. F. Valeev and H. F. Schaefer, *J. Chem. Phys.* **108**, 7197 (1998).
- ⁴⁸ A. A. Auer, T. Helgaker, and W. Klopper, *Phys. Chem. Chem. Phys.* **2**, 2235 (2000).
- ⁴⁹ D. J. Wales, *J. Chem. Phys.* **110**, 10403 (1999).
- ⁵⁰ Y. Xie, R. B. Remington, and H. F. Schaefer, *J. Chem. Phys.* **101**, 4878 (1994).
- ⁵¹ J. M. Headrick, E. G. Diken, R. S. Walters, N. I. Hammer, R. A. Christie, J. Cui, E. M. Myshakin, M. A. Duncan, M. A. Johnson, and K. D. Jordan, *Science* **308**, 1765 (2005).
- ⁵² M. Park, I. Shin, N. J. Singh, and K. S. Kim, *J. Phys. Chem. A* **111**, 10692 (2007).
- ⁵³ X. Huang, B. J. Braams, and J. M. Bowman, *J. Chem. Phys.* **122**, 044308 (2005).
- ⁵⁴ V. Kapil, J. VandeVondele, and M. Ceriotti, *J. Chem. Phys.* **144**, 054111 (2016).
- ⁵⁵ M. Ceriotti, D. E. Manolopoulos, and M. Parrinello, *J. Chem. Phys.* **134**, 084104 (2011).
- ⁵⁶ R. Kubo, *Reports on Progress in Physics* **29**, 255 (1966).
- ⁵⁷ M. Fixman, *Macromolecules* **19**, 1204 (1986).
- ⁵⁸ J. A. Izaguirre, D. P. Catarello, J. M. Wozniak, and R. D. Skeel, *J. Chem. Phys.* **114**, 2090 (2001).
- ⁵⁹ R. F. Fox, I. R. Gatland, R. Roy, and G. Vemuri, *Phys. Rev. A* **38**, 5938 (1988).
- ⁶⁰ R. D. Skeel and J. A. Izaguirre, *Molecular Physics* **100**, 3885 (2002).
- ⁶¹ A. Ricci and G. Ciccotti, *Molecular Physics* **101**, 1927 (2003).
- ⁶² E. Vanden-Eijnden and G. Ciccotti, *Chemical Physics Letters* **429**, 310 (2006).
- ⁶³ G. Bussi and M. Parrinello, *Phys. Rev. E* **75** (2007).

- ⁶⁴ S. Melchionna, J. Chem. Phys. **127**, 044108 (2007).
- ⁶⁵ N. Grønbech-Jensen and O. Farago, Molecular Physics **111**, 983 (2013).
- ⁶⁶ H. Dammak, Y. Chalopin, M. Laroche, M. Hayoun, and J.-J. Greffet, Phys. Rev. Lett. **103**, 190601 (2009).
- ⁶⁷ M. Ceriotti, G. Bussi, and M. Parrinello, Phys. Rev. Lett. **103** (2009).
- ⁶⁸ F. Briec, H. Dammak, and M. Hayoun, J. Chem. Theory Comput. **12**, 1351 (2016).
- ⁶⁹ M. Ceriotti, M. Parrinello, T. E. Markland, and D. E. Manolopoulos, J. Chem. Phys. **133**, 124104 (2010).
- ⁷⁰ J. Liu, D. Li, and X. Liu, J. Chem. Phys. **145**, 024103 (2016).
- ⁷¹ H. F. Trotter, Proc. Amer. Math. Soc. **10**, 545 (1959).
- ⁷² M. Parrinello and A. Rahman, J. Chem. Phys. **80**, 860 (1984).
- ⁷³ S. Nos, The Journal of Chemical Physics **81** (1984).
- ⁷⁴ W. G. Hoover, Phys. Rev. A **31**, 1695 (1985).
- ⁷⁵ M. Ceriotti, G. Bussi, and M. Parrinello, J. Chem. Theory Comput. **6**, 1170 (2010).
- ⁷⁶ F. Tassone, F. Mauri, and R. Car, Phys. Rev. B **50**, 10561 (1994).
- ⁷⁷ M. Tuckerman, B. J. Berne, and G. J. Martyna, The Journal of Chemical Physics **97** (1992).
- ⁷⁸ J. C. Sexton and D. H. Weingarten, Nuclear Physics B **380**, 667 (1992).
- ⁷⁹ D. M. Ceperley, Rev. Mod. Phys. **67**, 279 (1995).
- ⁸⁰ D. Marx, M. E. Tuckerman, J. Hutter, and M. Parrinello, Nature **397**, 601 (1999).
- ⁸¹ T. Spura, H. Elgabarty, and T. D. Kühne, Phys. Chem. Chem. Phys. **17**, 14355 (2015).
- ⁸² K. Suzuki, M. Tachikawa, and M. Shiga, J. Chem. Phys. **138**, 184307 (2013).
- ⁸³ M. Casula, C. Attaccalite, and S. Sorella, J. Chem. Phys. **121**, 7110 (2004).
- ⁸⁴ M. Burkatzki, C. Filippi, and M. Dolg, J. Chem. Phys. **126**, 234105 (2007).
- ⁸⁵ S. Sorella, N. Devaux, M. Dagrada, G. Mazzola, and M. Casula, J. Chem. Phys. **143**, 244112 (2015).
- ⁸⁶ M. Dagrada, M. Casula, A. M. Saitta, S. Sorella, and F. Mauri, J. Chem. Theory Comput. **10**, 1980 (2014).
- ⁸⁷ S. Sorella, Phys. Rev. B **64** (2001).
- ⁸⁸ C. J. Umrigar, J. Toulouse, C. Filippi, S. Sorella, and R. G. Hennig, Phys. Rev. Lett. **98** (2007).
- ⁸⁹ X. Cheng, J. D. Herr, and R. P. Steele, J. Chem. Theory Comput. **12**, 1627 (2016).
- ⁹⁰ I. Poltavsky and A. Tkatchenko, Chem. Sci. **7**, 1368 (2016).
- ⁹¹ T. E. Markland and D. E. Manolopoulos, Chemical Physics Letters **464**, 256 (2008).
- ⁹² T. E. Markland and D. E. Manolopoulos, J. Chem. Phys. **129**, 024105 (2008).
- ⁹³ G. S. Fanourgakis, T. E. Markland, and D. E. Manolopoulos, J. Chem. Phys. **131**, 094102 (2009).
- ⁹⁴ M. Ceriotti, G. Bussi, and M. Parrinello, Phys. Rev. Lett. **102** (2009).
- ⁹⁵ C. Filippi and C. J. Umrigar, Phys. Rev. B **61**, R16291 (2000).
- ⁹⁶ S. Sorella and L. Capriotti, J. Chem. Phys. **133**, 234111 (2010).
- ⁹⁷ Y. Luo, A. Zen, and S. Sorella, J. Chem. Phys. **141**, 194112 (2014).
- ⁹⁸ P. H.-L. Sit and N. Marzari, J. Chem. Phys. **122**, 204510 (2005).
- ⁹⁹ G. Mazzola and S. Sorella, Phys. Rev. Lett. **118**, 015703 (2017).